

Olivine-Based Cathode Materials

Karim Zaghib, Alain Mauger and Christian M. Julien

1 Introduction

The lithium insertion compounds built with polyanionic groups such as $(\text{SO}_4)^{2-}$, $(\text{PO}_4)^{3-}$, $(\text{P}_2\text{O}_7)^{4-}$, $(\text{MoO}_4)^{2-}$ or $(\text{WO}_4)^{2-}$ are considered as potential positive electrode materials for use in lithium rechargeable batteries [1, 2]. Yet in this family, olivine phosphate and Nasicon-like frameworks are currently the subject of many investigations. In particular, LiFePO_4 (LFP) has received a great deal of interest because this cathode material realizes the highest capacity ($\approx 170 \text{ mAh g}^{-1}$) at moderate current densities [3]. In addition, it presents several advantages with regard to low cost, non-toxicity, tolerance on abuse, and high safety, which are determinant with respect to cobalt-oxide-based materials for large-scaled applications such as hybrid electric vehicles (HEV). Nevertheless, the bulk electronic conductivity of olivine is quite low, which may result in losses in the specific capacity during high-rate discharge. To increase the electrochemical performance, it is a common practice in the production of Li-ion battery cathodes to manipulate the active material by (i) adding carbon additives to a olivine matrix [1, 4], (ii) surface coating of particles with thin layers of carbon [5–7] or reducing the particle size [8].

Still, there have been numerous efforts through the years to decrease the size of the particles from a few microns to this “nano” range, for several reasons. One is the increase of the effective contact area of the powder with the electrolyte. A larger effective contact surface with the electrolyte means a greater probability to drain Li^+

K. Zaghib (✉)
IREQ, Varennes, QC, Canada
e-mail: Zaghib.Karim@ireq.ca

A. Mauger
IMPMC, Université Pierre et Marie Curie, Paris, France

C.M. Julien
PHENIX, Université Pierre et Marie Curie, Paris, France
e-mail: christian.julien@upmc.fr

ions from the electrode, which increases the power density of the cell. A smaller particle size also reduces the length of the path of Li inside the particle, which leads to a greater capacity at higher charge/discharge rates and therefore to a larger power density. Reducing the dimensions of the active particles to nanoscale means, for a given chemical diffusion coefficient of Li^+ ions, D^* , the characteristic time, τ_c , for the intercalation reaction is given by the Fick's law. For non stoichiometric system (one-phase reaction) the characteristic time constant for is expressed by:

$$\tau_c = L^2/4\pi D^*, \quad (1)$$

where L is the diffusion length [9]. In the case of olivine compounds, the insertion operates through a two-phase process, so the characteristic time constant becomes:

$$\tau_c = \frac{F^2}{2V_m} \frac{L^2}{\langle \sigma^i \rangle \Delta \mu_i}, \quad (2)$$

in which F is the Faraday constant, V_m the molar volume, σ^i the ionic conductivity and $\Delta \mu_i$ the chemical potential of ions. Nanoparticles, as well as more tailored nanostructures, are being explored and exploited to enhance the rate capability, even for materials with poor intrinsic electronic conductivity such as olivine frameworks. In addition, the problems raised by the small electronic conductivity that results from the strong ionicity of the bonding have been solved by coating the olivine particles with a thin layer that is conductive for both electrons and Li, usually an amorphous carbon layer [10, 11]. Decreasing the particle size reduces the length of the tunneling barrier for electrons to travel between the surface layer and the core of the particle, while the electrons are driven from the surface of the particle to the current collector via the conductive layer that percolates through the structure. The coat may also decrease the activation energy for Li^+ transfer across the electrode/electrolyte interfaces. Indeed, by preparing the materials at the nanoscale form and by carbon coating, high rates are achievable [10].

The aim of the present chapter is to investigate the physicochemical properties of optimized olivine-like electrode materials. One approach to provide insight into the structural and electronic properties of electrode materials involves a systematic study by a combination of techniques including structural, magnetic and spectroscopic measurements. Furthermore, advantage can be taken of the high sensitivity of some analytical tools for the detection of parasitic impurities that can be grown during synthesis of solid phases. These principles were fully exploited to optimize lithium iron phosphate compounds. This chapter is organized as follows. First, we expose in Sect. 2 the principle of the inductive effect in polyanionic frameworks. Section 3 presents the synthesis route, the structure and morphology of optimized LiFePO_4 particles probed by X-ray powder diffractometry (XRD), Scanning Electron Microscopy (SEM), High Resolution Transmission Electron Microscopy (HRTEM), Fourier transform infrared (FTIR) and Raman scattering (RS) spectroscopy. We then complete the analysis (Sect. 4) with magnetic measurements: magnetization curves and electron spin resonance (ESR). In Sect. 5, we examine the

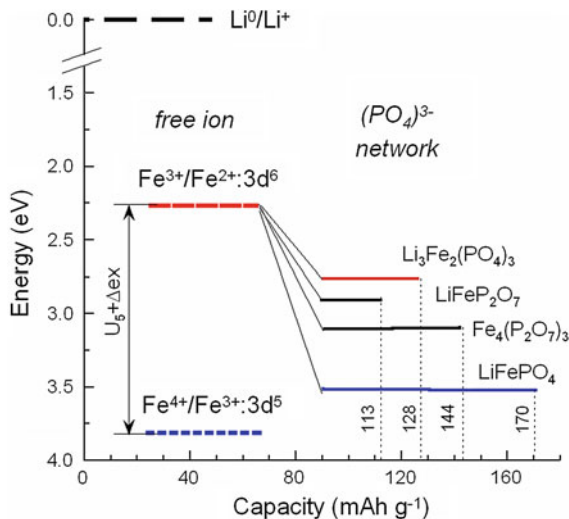
electrochemical properties of LFP in various situations including high temperature, high current density, and in humid atmosphere. In the following Sects. 6–8, we explore the other olivine materials, namely LiMnPO_4 , LiNiPO_4 and LiCoPO_4 .

2 The Inductive Effect

The aspect of tuning the redox potential of an electrode material has been demonstrated by Goodenough et al. [1, 2, 12–14]. They have shown that the use of polyanions $(\text{XO}_4)^{n-}$ such as $(\text{SO}_4)^{2-}$, $(\text{PO}_4)^{3-}$, $(\text{AsO}_4)^{3-}$, or even $(\text{WO}_4)^{2-}$ lowers the redox energy of the $3d$ -metals to useful levels with respect to the Fermi level of the Li anode. Thus, the most attractive key point of the polyanion frameworks can be seen in the strong X–O covalency, which results in a decrease of the Fe–O covalency. This inductive effect is responsible for a decrease of the redox potential in comparison to the oxides [12]. The polyanion PO_4^{3-} unit stabilizes the olivine structure of LiFePO_4 and lowers the Fermi level of the $\text{Fe}^{2+/3+}$ redox couple through the Fe–O–P inductive effect which results in a higher potential for the olivine material. The discharge voltage 3.45 V is almost 650 mV higher than that of $\text{Li}_3\text{Fe}_2(\text{PO}_4)_3$ [1]. It is also 350 mV higher than that of $\text{Fe}_2(\text{SO}_4)_3$ [14], which is consistent with the stronger Bronsted acidity of sulphuric versus phosphoric acid. In the case of $\text{Li}_2\text{FeSiO}_4$, the lower electronegativity of Si versus P results in a lowering of the $\text{Fe}^{2+/3+}$ redox couple [15]. On the other hand, the higher thermal stability of the phospho-olivines and their lower tendency to release oxygen is explained by the strong X–O covalency and the rigidity of the $(\text{XO}_4)^{n-}$ units decreasing the safety risks. However, AMXO_4 compounds and $\text{AM}(\text{XO}_4)_3$ as well (A is an alkali ion) exhibit a very low electronic conductivity because of the separation between MO_6 octahedra and XO_4 tetrahedra that induces a large polarization effect during charge–discharge reaction [16].

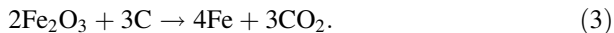
Electrochemical extraction of Li from LiFePO_4 gives $(\text{Fe}^{2+}/\text{Fe}^{3+})$ redox potential at ca. 3.5 V versus Li^0/Li^+ . A small but first-order displacive structural change of the framework gives a two-phase separation over most of the solid-solution range $0 < x < 1$ for Li_xFePO_4 and therefore a flat V - x curve. A reversible capacity of 160 mAh g^{-1} is delivered by the nano-structured cathode particles coated with carbon. Electrochemical characteristics of LiFePO_4 are compared with those of other Fe-containing phosphates in Fig. 1. This graph presents the energy of the redox couples against the specific capacity relative to lithium and iron in various phosphate frameworks. Electrochemical tests of optimized LiFePO_4 have been conducted under various conditions to assess the influence of the electrolyte on stability and the influence of electrode processing. Post-mortem analysis, i.e. ICP, XRD, SEM, showed that no iron species were detected at the separator-negative electrode interface in cells with anode in lithium metal, graphite, or $\text{C-Li}_4\text{Ti}_5\text{O}_{12}$ [17, 18]. This result is attributed to the high quality of the “optimized” LiFePO_4 , impurity-free materials used as positive electrodes. This property characterizes the impact of structural fluorine on the inductive effect of the PO_4^{3-} polyanion.

Fig. 1 Energy diagram of the redox couple relative to lithium and iron phosphate frameworks. The graph presents the theoretical capacity for each compound



3 Lithium Iron Phosphate

The electrochemical properties of LFP are known to be sensitive to the mode of preparation and the structural properties [19]. This can be an advantage for potential applications since it allows for an optimization of the material if we can correlate the mode of preparation with the structural and the physical properties. Aiming to this problem, we have first investigated this correlation in LiFePO_4 grown by different techniques [20–24]. Different clustering effects have been evidenced [19]. A firing temperature larger than 800 °C increases the fraction of Fe_2P [25], but Fe_2P nano-particles in such a large concentration that they drive superferromagnetism has been detected in samples that have not been heated to such high temperatures [20]. On the one hand, the presence of Fe_2P can increase the electronic conductivity, but on the other hand it also decreases the ionic conductivity so that both the capacity and cycling rates are degraded with respect to the carbon-coated LFP. It is thus desirable to optimize the preparation of the samples so that such clustering effects do not occur. This can be done easily for Fe_2P clusters, but it is more difficult to avoid the presence of a small concentration (1.0×10^{-6} per chemical formula) of $\gamma\text{-Fe}_2\text{O}_3$ nanoparticles [20, 26] in carbon-free LFP. However, we know from the iron industry that hydrogen, carbon monoxide or carbon can reduce Fe_2O_3 through different reduction steps that depend on temperature and other physical parameters such as particle sizes. Nearly all iron produced commercially is made using a blast furnace process covered by most chemistry text books. In essence, at high temperature, Fe_2O_3 , is reduced with carbon (as coke) according to the reaction:



This is one of the most significant industrial processes in history, and the origins of the modern process are traceable back to a small town called Coalbrookdale in Shropshire (England) around the year 1773. We can then expect that carbon would reduce Fe^{3+} ions directly or through the formation of CO gas thus preventing the formation of $\gamma\text{-Fe}_2\text{O}_3$, if the synthesis temperature might be raised to 1000 °C. However, such a high temperature is prohibited to synthesize nano-LFP. We believe that the carbon deposition process using organic carbon precursors generates reductive gases such as hydrogen that are more active kinetically to reduce Fe^{3+} impurities in the 500–700 °C temperature range used. This is also favored by the fact that the organic precursor is usually mixed with the LFP material or with the LFP chemical precursors by solution processes at a molecular size level. For overview on olivine phosphate material see the reviews recently published [17, 19, 27].

3.1 Synthesis Routes

Many synthesis routes have been used for the preparation of LFP materials [21–48]. Here, we will focus on three methods used by our group: solid-state, hydrothermal and jet milling techniques [21–23]. Then a comparison of the physical and electrochemical properties of a series of carbon-coated LiFePO_4 is used to optimize the materials for battery application. Precursors were prepared by mixing various raw materials: iron(II) oxalate $[\text{Fe}(\text{C}_2\text{O}_4)_2 \cdot \text{H}_2\text{O}]$ or $[\text{FePO}_4(\text{H}_2\text{O})_2]$, ammonium dihydrogen phosphate $[\text{NH}_4\text{H}_2\text{PO}_4]$ and lithium salt $[\text{Li}_2\text{CO}_3]$ or $[\text{LiOH}]$. The chemical homogeneity and purity of the powders appear to be sensitive to the conditions of preparation. Thus, the choice of the raw materials, carbon precursor, temperature, and atmosphere is required not only for the reduction of Fe(III) but also for the carbon-coating formation.

A solid-state synthesis method assisted by polymeric carbon additive proved to be efficient to prepare LFP at quite low temperature, 300–400 °C, while the sintering temperature that does not exceed 750 °C makes the existence of any carbonothermal effect unlikely [28]. A blend of $\text{Fe}^{\text{III}}\text{PO}_4(\text{H}_2\text{O})_2$ and Li_2CO_3 was mixed by ball milling in isopropyl alcohol (IPA) overnight; the blend was dried and mixed with 5 wt% of a polymeric carbon additive, polyethylene-block-poly(ethylene glycol) 50 % ethylene oxide. Overall synthesis was carried out under flowing argon. Note that the carbon source could provide the LFP powder with a carbonaceous deposit after pyrolysis and such a powder pressed at 3750 kg cm^{-2} at room temperature presents an electronic conductivity much higher than $1 \times 10^{-8} \text{ S cm}^{-1}$ [11]. Other elements that can be present are hydrogen, oxygen, and nitrogen, as long as they do not interfere with the chemical inertia of the carbon. Preferred polymeric additives include, but are not limited to, hydrocarbons and their derivatives, especially those comprising polycyclic aromatic moieties, e.g. polyolefins,

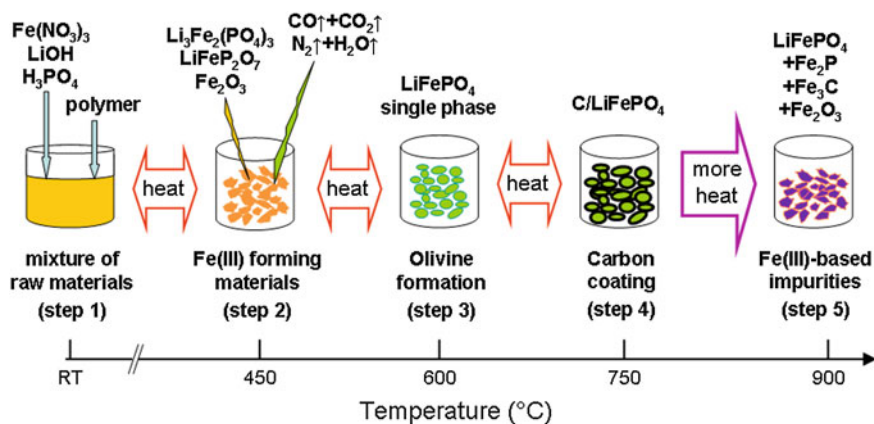


Fig. 2 Scheme of the steps of the polymer-assisted solid-state synthesis of LFP powders. The in situ carbon-coating is realized by polymer precursor at temperature $T_s < 750$ °C

polybutadienes, polyvinyl alcohol, etc. [11]. Figure 2 shows the different steps of the synthesis of carbon-coated LFP particles using the polymer-assisted solid-state method. Note that for $T_s > 750$ °C Fe(III)-containing impurities are formed that poison the electrochemical performance of LFP.

For some of the synthesis routes, the reduction to small size occurs at the expense of crystallinity and the formation of a large concentration of defects [29]. These difficulties have been overcome in the framework of a preparation process in which the mechanical assistance is used only to reduce the size of the particles [11]. In a first step, LFP particles were prepared by melting precursors at 1050 °C for 5 min in a graphite crucible and then cooled under N_2 atmosphere fast enough so that impurities have no time to nucleate [21]. The next step is to decrease the size of the particles down to the desired value, anywhere in the range from the centimeter down to 40 nm (Fig. 3). For this purpose, the ingot is first crushed into centimeter-size particles by using a jaw-crusher with ceramic liner to avoid metal contamination. Then, the roll crusher (ceramic type) is used to obtain millimeter-size particles. The millimeter-size particles are further ground by jet-mill to achieve micrometer-size particles. In the process, the grains enter the grading wheel and are blasted to the collector. The particles obtained at this step are referred as “jet-mill” in the following. Their size is the order of 1 μm . To obtain smaller particles, these micrometer-size powders were dispersed in isopropyl alcohol (IPA) solution at 10–15 % of solid concentration and then ground on a bead mill using 0.2-mm zirconia beads to obtain nanometer-sized particles [11]. This final product is referred “wet mill” in the following. One advantage of the process is that we can investigate the properties of the same particles at different stages of the milling, for comparison, so that any difference is a size effect. The particles can be considered as uncoated particles because of the great damage caused by the milling process. In the case of the particles used to obtain the experimental results illustrated in the figures of this

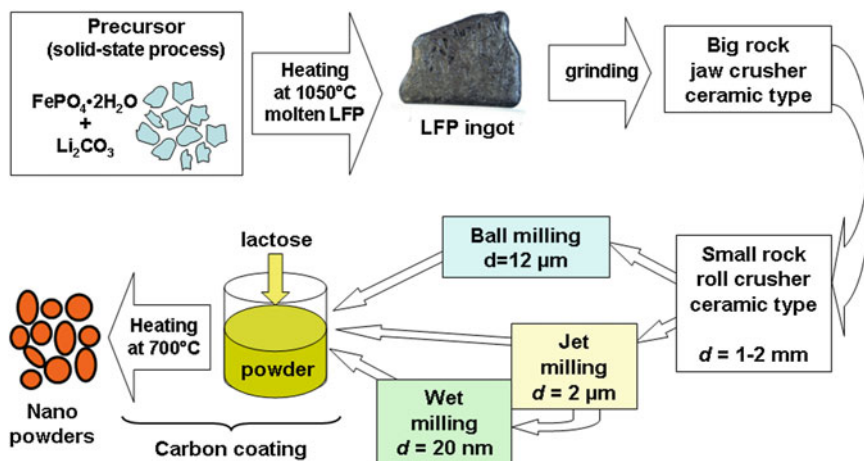


Fig. 3 Milling synthesis from molten ingot. Nanopowders are obtained using crusher ceramic liner and jet milling

review, the carbon-coated particles have been obtained with lactose as the carbon precursor in acetone solution according to the following procedure. The uncoated particles were mixed with the carbon precursor. The dry additive corresponded to 5 wt% carbon in LiFePO_4 . After drying, the blend was heated at 750 or 700 °C [21, 30] for 4 h under argon atmosphere. This range of temperature is dictated by two considerations. Below 700 °C, the carbon deposit was not conductive enough [21].

The hydrothermal route is particularly successful to control the chemical composition and crystallite size [28, 37–39]. The conventional hydrothermal process involves a reaction time 5–12 h to synthesize LFP [40, 41]. With respect to the previous techniques, the hydrothermal process has the advantage that the synthesis temperature can be as small as 230 °C [42]. Brochu et al. [23] demonstrated the beneficial effect of choosing adapted complexing agent in the hydrothermal solution. Even at this mild temperature the carbon coating of the particles could be achieved by an in situ hydrothermal carbonization of glucose during the synthesis process. The heating temperature to get the particles coated with conductive carbon was still 700 °C, but good results were obtained upon heating during one hour only. Carbon-coated LFP was prepared by hydrothermal synthesis assisted by rotating/stirring tests at different agitation speeds [24]. The process was carried out at 190 °C for 12 h with a solution chemistry of $\text{LiOH} \cdot \text{H}_2\text{O}$, $\text{FeSO}_4 \cdot 7\text{H}_2\text{O}$, H_3PO_4 (85 wt%), and ascorbic acid (as reducing agent) in the stoichiometry $3\text{Li}:1\text{Fe}:1\text{P}:0.2\text{C}$. Annealing was done at 700 °C under nitrogen atmosphere using lactose as carbon coating source. The $\text{LiFePO}_4\text{-C}$ electrodes prepared by employing agitation during hydrothermal synthesis were found to exhibit higher discharge capacities ($\sim 137 \text{ mAh g}^{-1}$ at C/12) than those prepared without agitation ($\sim 106 \text{ mAh g}^{-1}$). This was equally true for higher current rates, namely C/5 and C/3. Via a series of tests at different speeds (260–1150 rpm) and different concentrations (0.4–0.6 mol.

dm^{-3}) the optimum solution rotating agitation/concentration conditions were determined to be 260–380 rpm and 0.5 mol.dm^{-3} , respectively [24].

A polyol process to synthesize LFP has been developed first by Kim to synthesize particles under the form of rods with average width 20 nm and length 50 nm [37], but different shapes ranging from rods to plates can be obtained [38] with average size of 100–300 nm. Note the polyol process make possible the synthesis of LFP at low temperature just like the hydrothermal process. Bigger particles can be obtained by the solvothermal process in a polyol medium of diethylene glycol, but still under the form of plates or rods. The advantage of this process is that the polyol medium acts not only as a solvent, but also as a reducing agent and stabilizer that limits the particle growth and prevents agglomeration [38–40]. In general, the solvothermal process leads to the formation of LFP under the form of plates, about 50 nm-thick [41], which can be self-assembled by using poly(vinyl pyrrolidone) (PVP) as the surfactant in a benzyl alcohol system [42].

3.2 Structure of Olivine Phosphate

Triphylite is a rather scarce orthophosphate primary mineral found in phosphatic pegmatites and pegmatitic dikes. Its formula is $\text{Li}(\text{Mn,Fe})\text{PO}_4$ and differs from the other mineral, lithiophilite, by being rich in iron instead of manganese. The structures of the two minerals are the same and form a solid solution, referred as the triphylite series, isomorphous with olivine. Therefore, any differences in physical properties between the two would be related to the iron/manganese percentage. These differences are then best evidenced by comparing the physical properties of the two members at the opposite edges of the triphylite family, namely LiFePO_4 and the often associated material LiMnPO_4 (LMP), which, in contrast with triphylite and lithiophilite, are artificial ceramics [43]. In addition, triphylite's name in Greek means "family of three" (referring to Fe, Mn, and Li). Any confusion between LiFePO_4 and triphylite met recently in the literature should then be avoided. Triphylite alters easily into other phosphate minerals, and geologists show it a lot of respect for making the other phosphate minerals possible. This easy alteration, however, means that this material is not very stable and that it is difficult to make good quality, well-crystallized samples. Despite this drawback, many efforts have been focused on the definite compounds LFP and LMP rather than their solid solutions. They belong to the rich family of olivines of the Mg_2SiO_4 -type with the general formula $B_2\text{AX}_4$ [44].

The crystal structure of olivine materials has been studied by several authors [44, 48]. LiFePO_4 crystallizes in the orthorhombic system (No. 62) with $Pnma$ space group. It consists of a distorted hexagonal-close-packed oxygen framework containing Li and Fe located in half the octahedral sites and P ions in one-eighth of the tetrahedral sites [46]. The FeO_6 octahedra, however, are distorted, lowering their local cubic-octahedral O_h to the C_s symmetry. Corner-shared FeO_6 octahedra are

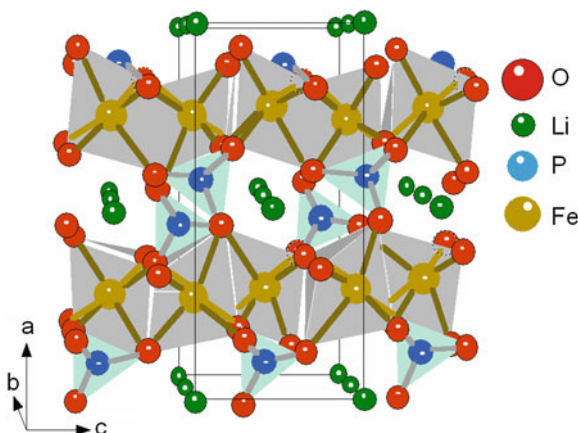


Fig. 4 Crystal structure of LiFePO_4 olivine. Corner-shared FeO_6 octahedra are linked together in the bc -plane; LiO_6 octahedra form edge-sharing chains along the b -axis. The tetrahedral PO_4 groups bridge neighboring layers of FeO_6 octahedra by sharing a common edge with one FeO_6 octahedra and two edges with LiO_6 octahedra

linked together in the bc -plane; the LiO_6 octahedra form edge-sharing chains along the b -axis. The tetrahedral PO_4 groups bridge neighboring layers of FeO_6 octahedra by sharing a common edge with one FeO_6 octahedron and two edges with LiO_6 octahedra. Remarkably short O–O bonds at the shared PO_4 and FeO_6 edges help to screen the cation charges from each other. This structure is illustrated in Fig. 4 showing the 1-D channels via which the lithium ions can be removed. Corner-shared FeO_6 octahedra are linked together in the bc -plane, while LiO_6 octahedra form edge-sharing chains along the b -axis. The tetrahedral PO_4 groups bridge neighboring layers of FeO_6 octahedra by sharing a common edge with one FeO_6 octahedra and two edges with LiO_6 octahedra.

The LiFePO_4 structure consists in three non-equivalent O sites. Most of the atoms of the olivine structure occupy the $4c$ Wyckoff position except O(3) that lies in the general $8d$ position and Li^+ ions occupying only the $4a$ Wyckoff position (M1 site on an inversion center). The Fe magnetic ions are in the divalent Fe^{2+} state of the FeO_6 units. As a consequence, Fe is distributed so as to form FeO_6 octahedra isolated from each other in TeO_2 layers perpendicular to the (001) hexagonal direction [47]. In addition, the lattice has a strong two-dimensional character, since above a TeO_2 layer comes another one at the vertical of the previous one, to build (100) layers of FeO_6 octahedra sharing corners and mixed layers of LiO_6 octahedra. Nevertheless, these Fe–O planes are strongly linked by the PO_4 bridges, so that the material is truly three-dimensional, which insures the remarkable thermal stability with respect of the lamellar compounds. The synthetic lithium iron phosphate material differs from the primary mineral triphylite $(\text{Mn,Fe})\text{PO}_4$ by the fact that triphylite is only rich in iron, with some manganese ions also in the M2 site. However, while the triphylite is a naturally occurring mineral, LiFePO_4 is an

Table 1 Lattice constants for stoichiometric LiFePO_4 materials in the $Pnma$ (62) structure

a (Å)	b (Å)	c (Å)	Unit cell volume (Å ³)	Refs.
10.332(4)	6.010(5)	4.692(2)	291.4(3)	Herle [25]
10.334	6.008	4.693	291.39	Yamada [52]
10.329(0)	6.006(5)	4.690(8)	291.02	Geller [44]
10.31	5.997	4.686	289.73	Santoro [45]
10.3298	6.0079	4.6921	291.19	Andersson [53]
10.334(4)	6.008(3)	4.693(1)	291.392(3)	Padhi [1]

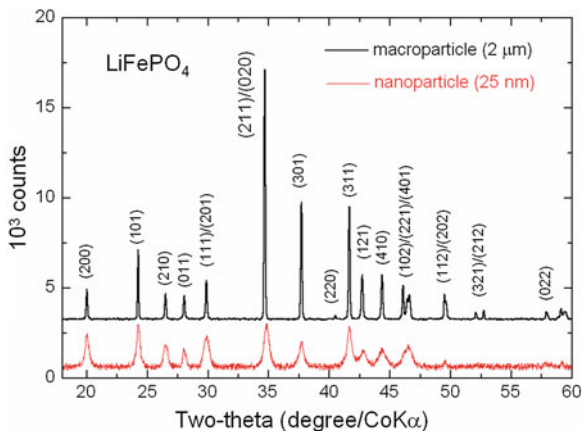
Table 2 Fractional coordinates and site symmetry of atoms in LiFePO_4 ($Pnma$)

Atom	x	y	z	Site symmetry
Li	0	0	0	$\bar{1}$ ($4a$)
Fe	0.28222	$\frac{1}{4}$	0.97472	m ($4c$)
P	0.09486	$\frac{1}{4}$	0.41820	m ($4c$)
O(1)	0.09678	$\frac{1}{4}$	0.74279	m ($4c$)
O(2)	0.45710	$\frac{1}{4}$	0.20602	m ($4c$)
O(3)	0.16558	0.04646	0.28478	1 ($8d$)

artificial product. On a fundamental point of view, the main interest lies in the fact that the olivine structure generates magnetic-interaction frustration [49]. However, three olivine structure classes can be distinguished as a function of the site occupation by magnetic ions. In Mn_2SiS_4 and Fe_2SiS_4 , the magnetic ion (Mn, Fe) lies in the $M1$ and the $M2$ site [50], while in NaCoPO_4 and NaFePO_4 , the magnetic ion lies on the $M1$ site only [51]. The third class is the phospho-olivine LiMPO_4 ($M=\text{Ni, Co, Mn, Fe}$) where the magnetic ion lies in the $M2$ site with the $M1$ site occupied by the non-magnetic ion (Li^+).

We used the recent structure determination by Streltsov et al. [46] as a standard reference (Table 1). The orthorhombic unit cell of the olivine structure contains 28 atoms ($Z = 4$). Structural parameters are listed in Table 2. Fe–O distances range from 2.064 to 2.251 Å. The Fe–Fe separation in LiFePO_4 is large (3.87 Å). The magnetic interactions between Fe ions are antiferromagnetic superexchange interactions of the form $-\text{Fe}-\text{O}-\text{Fe}-$ and $-\text{Fe}-\text{O}-\text{P}-\text{O}-\text{Fe}-$, consistent with the antiferromagnetic ordering observed below $T_N = 52$ K [43]. Figure 5 shows the typical XRD spectra of two LiFePO_4 samples with nano- and micro-sized particles. Crystallite sizes 25 nm and 2 μm were estimated using the Scherrer formula.

Fig. 5 XRD patterns of LFP samples with nano-sized particles (lower spectrum) obtained after jet milling and micro-sized particles (upper spectrum). Note the large broadening of the XRD lines of the nano-sized particles



3.3 Morphology of LFP

The surface morphologies of the nano-sized LFP powders studied by HRTEM are reported in Fig. 6. The powders are composed of well-dispersed secondary particles that are slightly agglomerated, with a small quantity of fragments. The TEM pictures show similar images at any part of the sample, which is homogeneous at the nanoscale with respect to the area investigated. Images (a and b) are then representative of the free-carbon particles with the tendency of forming agglomerates. Each of the secondary particles is made of a large number of small primary particles. The HRTEM images (c and d) for the carbon-coated sample illustrated poly-dispersed primary particles with a mean size ≈ 90 nm, which is larger by a factor 3 with respect to the average size of the monocrystallite grains deduced from the application of the Scherrer law on the XRD pattern. Therefore, the primary particles are polycrystallites of LiFePO_4 made of a few (3 on average) monocrystallites of LiFePO_4 . The amorphous carbon layer is well illustrated in the TEM pictures (Fig. 6c, d). The formation of a carbon network appears in the interstitial grain-boundary region, which could explain the electrical continuity between LiFePO_4 crystallites. In the micrographs, the LiFePO_4 crystallites appear as the darker regions while the carbon coating is surrounding the primary particle as the greyish region. The average thickness is estimated to be 30 nm. The carbon film is highly porous, which results in an irregular coating of the crystallites well-observed on the HRTEM images but the important point for the electronic conductivity is that it connects the particles. To summarize these results, the HRTEM images clearly depict the beneficial effect of a carbon layer coating the LFP crystallites. XRD and HRTEM data are consistent.

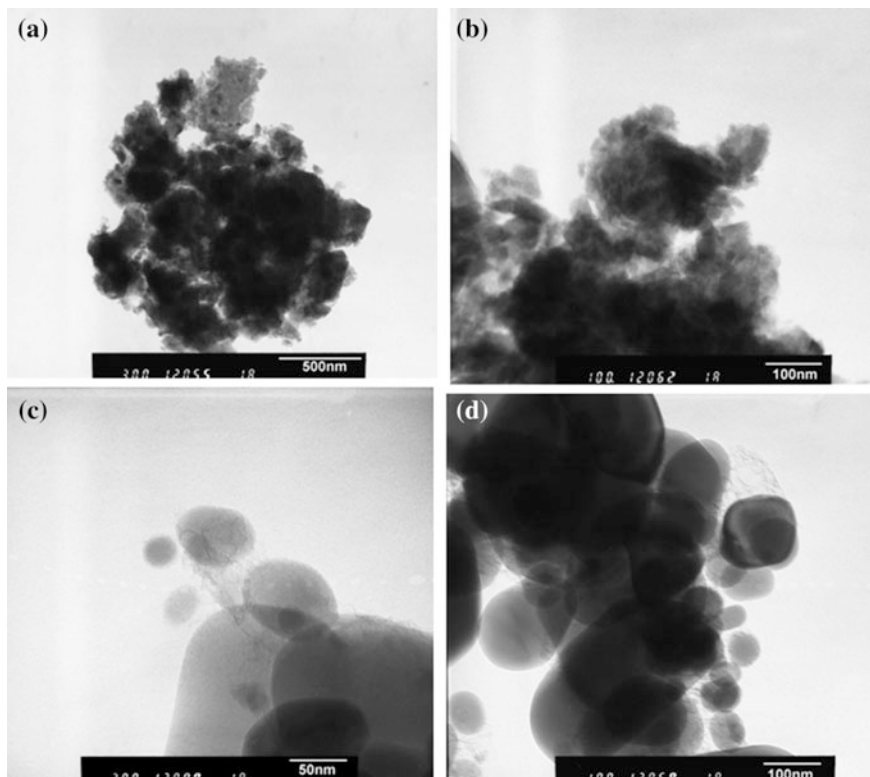
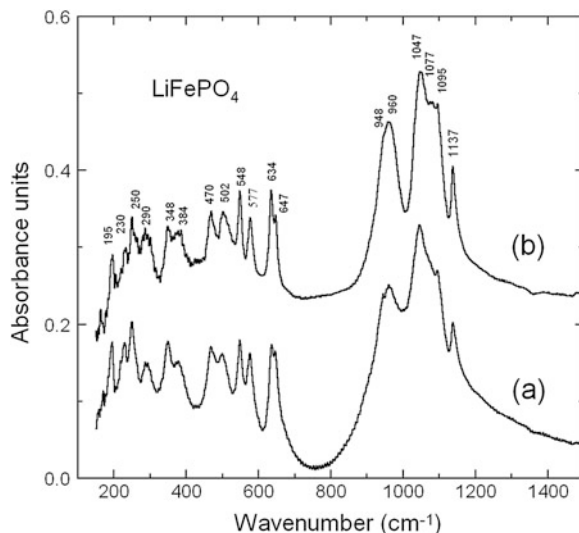


Fig. 6 HRTEM images of LFP nano-sized particles (a, b) before carbon coating and (c, d) after carbon deposited by the lactose method

3.4 Local Structure, Lattice Dynamics

Fourier transform infrared (FTIR) spectroscopy probes bulk properties, while Raman scattering (RS) spectroscopy is the tool to perform surface analysis [54–57]. For instance, the amount of carbon on LiFePO_4 is too small to be detected by FTIR, but it is well-characterized by RS experiments [54]. The vibrational modes of LiFePO_4 are primarily due to motion associated with phosphate and iron the other modes show some lithium contribution [55]. The FTIR spectra of the samples are reported in Fig. 7. We have also reported the position of the peaks intrinsic to this material, already identified in earlier works [52]. Let us recall that the spectra result from absorption measurements, so that they are a probe of the bulk properties, and the amount of carbon in the material is too small to be detected by such experiments. This is the basic reason why the FTIR spectra are characteristics of the LiFePO_4 part. The positions of all the IR bands are in agreement with those in Ref. [58]. No extra line is observed with respect to pure LFP. The bands in the range $372\text{--}647\text{ cm}^{-1}$ are bending modes (ν_2 and ν_4) involving O–P–O symmetric and

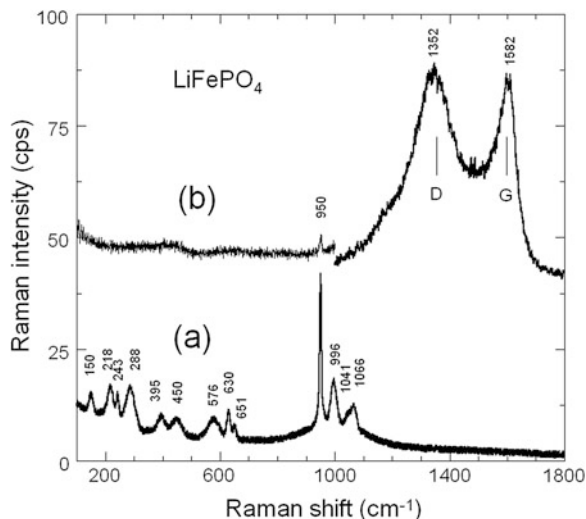
Fig. 7 FTIR absorption spectra of (a) carbon-free and (b) carbon-coated LiFePO_4 samples. Peak positions are marked (in cm^{-1}). Infrared spectra were recorded on pellet of LiFePO_4 powders diluted into ICs matrix (1:300)



asymmetric modes and Li vibrations [55]. In particular, the line at 230 cm^{-1} corresponds to the same cage mode of the lithium ions that undergo translation vibrations inside the cage formed by the six nearest-neighbour oxygen atoms [56]. The bands in this range $372\text{--}647\text{ cm}^{-1}$ are thus the part of the spectrum that is sensitive to the local lithium environment. This is also the part of the spectrum that is the same in both the carbon-free and carbon-coated samples. We can then infer from this result that the lithium ions do not ‘see’ the carbon ions, another evidence that the carbon did not penetrate inside the LFP particles. The part of the spectrum in the range $945\text{--}1139\text{ cm}^{-1}$ corresponds to the stretching modes of the $(\text{PO}_4)^{3-}$ units. They involve symmetric and asymmetric modes of the P–O bonds at frequencies closely related to those of the free molecule, which explains that the frequencies of these modes are the same in both samples. However, the modes in the carbon-free sample are significantly broader than in the carbon-coated sample. This broadening gives evidence of a decrease in the lifetime of the phonons, and thus the existence of defects breaking the periodicity of the lattice sites inside the LFP crystallites of the carbon-free sample. The analysis of magnetic properties in the next section will allow us to identify these defects as $\gamma\text{-Fe}_2\text{O}_3$ nanoparticles.

To explore the surface properties of the LFP particles, Raman spectra have been measured; the penetration depth for carbon with Raman spectroscopy is approximately 30 nm [54]. This is one order of magnitude larger than the thickness of the carbon coat deposited at the surface of the LFP particles in case of a uniform carbon distribution. Therefore, any screening effect of carbon on the LiFePO_4 spectra is not expected. The penetration depth inside LiFePO_4 is unknown, but it should be small, so that the detector in the Raman experiments collects the signal within the light penetration depth, which basically represents the total amount of carbon and a few per cent of the amount of LiFePO_4 . Since the total amount of carbon is itself $5\text{ wt}\%$

Fig. 8 Raman spectra of the carbon-free and carbon-coated LiFePO_4 samples. Spectra were recorded using the 514.5 nm laser line at the spectral resolution 2 cm^{-1} . RS features of the LiFePO_4 bulk material are screened by the carbon deposit for which the G- and D-band are observed



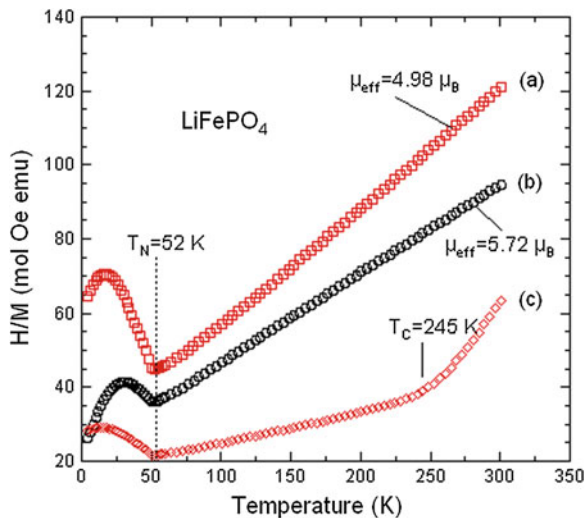
of LiFePO_4 , we can expect that comparable amounts of carbon and LiFePO_4 are probed by the sampling depth. This is confirmed by the Raman spectra reported in Fig. 8. The part of the spectrum in the wave number range $100\text{--}1100\text{ cm}^{-1}$ is the same in the carbon-free and the carbon-coated sample and only the lines characteristics of LiFePO_4 are detected in this range. The peak positions reported in Fig. 8 in this range are within a few cm^{-1} the same as those that have been reported in [57], and we refer to this prior work for their assignment. The largest difference is for the line at 395 cm^{-1} , which is reported at 410 cm^{-1} in Ref. [55]. This line is associated with the PO_4 bending modes ν_2 , ν_4 which are strongly coupled. However, we cannot consider this difference as significant since all the other lines associated with PO_4 have the same position. This is the case in particular for the lines at 620 , 940 , 986 and 1058 cm^{-1} associated with ν_4 , ν_1 , ν_3 and ν_2 intramolecular stretching modes of PO_4 , respectively. The only difference in this range of wave numbers is a shift of the Raman lines by about 10 cm^{-1} towards lower frequencies in the carbon-coated sample. This shift of the Raman lines is in contrast with the absence of any shift of the FTIR lines, which gives evidence that it is a surface effect. This shift of the Raman lines is attributable to the increase of the bonding length in the first layers of LFP_4 particles near the interface with the carbon, taking its origin in the strain induced by the adhesion of the carbon film. For samples with a different mode of preparation, carbon was reported to be responsible for a screening of the signal from bulk, so that only a weak band at 942 cm^{-1} associated with LFP could still be detected [54]. Again, such a screening is not expected for the reasons above mentioned, and it is not observed in the present case.

3.5 Iron(III) Nanoclusters in LFP

Recently, significant effort has been underway to improve LiFePO_4 by developing a new synthesis route via carbon coating [59, 60]. The 1-D Li channels make the olivine performance sensitive not only to particle size, but also to impurities and stacking faults that block the channels. Various types of iron-based impurities have been identified in the olivine framework: for examples $\gamma\text{-Fe}_2\text{O}_3$, Fe_3O_4 , $\text{Li}_3\text{Fe}_2(\text{PO}_4)_3$, $\text{Fe}_2\text{P}_2\text{O}_7$, Fe_2P , Fe_3P , $\text{Fe}_{75}\text{P}_{15}\text{C}_{10}$, etc. Critical quality control of the product is necessary to obtain a complete understanding of synthesis conditions using combination of experiments such as Raman spectroscopy and magnetic measurements [20–22, 59, 60]. Analysis of the magnetic properties gives an average separation of the magnetic clusters that is too large for interaction between particles (superparamagnetic model). This hypothesis must be released where the number n of magnetic clusters of momentum μ is so large that magnetic interactions between the ferrimagnetic particles become important [20]. At high fields, M_{extrin} saturates to $Nn\mu$ so that this quantity is readily determined as the magnetization at the intersection of the tangent to the magnetization curves at large fields with the ordinate axis at $H = 0$. As a result, we find that $Nn\mu$ does not depend significantly on temperature below 300 K. Therefore, we are in the situation where the cluster magnetization is temperature independent, which amounts to say that the Curie temperature T_c inside the clusters is much larger than 300 K. This is an important information on the nature of the ferromagnetic clusters. In particular, this feature precludes the existence of Fe_2P clusters observed in some LFP samples prepared according to a different procedure [59], since the Curie temperature of these clusters is only 220 K. The nature of the strongly ferromagnetic clusters in the present case is most likely maghemite ($\gamma\text{-Fe}_2\text{O}_3$).

It is remarkable from Fig. 9 that the synthesized LFP sample displays different magnetic features, with a magnetic moment $\mu_{\text{eff}} = 5.72 \mu_B$ due to the existence of Fe (III) containing impurities. The first consequence is an ambiguity in what is called the magnetic susceptibility χ_m since M/H is distinct from dM/dH . The magnetic susceptibility measured with a SQUID at $H = 10$ kOe shows the non-linearity of the magnetic moments attributed to the presence of $\gamma\text{-Fe}_2\text{O}_3$. The best material shows the lowest Curie constant $3.09 \text{ emu K mol}^{-1}$. The effective magnetic moment $\mu_{\text{eff}} = 4.98 \mu_B$ is close to theoretical value $4.90 \mu_B$ calculated from the spin-only value of Fe^{2+} in its high-spin configuration. Departure from the spin-only value is attributable to the presence of Fe^{3+} ions because the orbital-momentum contribution of the Fe^{2+} ions is quenched by the crystal field [26].

Fig. 9 Temperature dependence of the reciprocal magnetic susceptibility of different LiFePO_4 samples. (a) optimized pure LiFePO_4 , (b) Fe_2O_3 -containing sample, and (c) $\chi^{-1}(T)$ of Fe_2P -containing sample. μ_{eff} is deduced from the Curie-Weiss law $\chi = C/(T + \theta)$ above the Néel temperature T_N



3.6 Influence of the Fe_2P Nanoclusters

The electrochemical properties of LFP are known to be sensitive to the mode of preparation and the structural properties [61]. This can be an advantage for potential applications since it allows for an optimization of the material if we can correlate the mode of preparation with the structural and the physical properties. To address this issue, we investigated this relationship in LiFePO_4 samples grown under different conditions [62]. Undesirable impurities in the lattice can be introduced during the growth process. For instance, the presence of Fe_2P can increase the electronic conductivity, but on the other hand it also decreases the ionic conductivity so that both the capacity and cycling rates are degraded with respect to C-LFP. In addition, the iron from Fe_2P dissolves into the electrolyte, which reduced the calendar life of the cell. The presence of a small concentration ($>0.5\%$) of Fe_2P is evidenced in Fig. 9 by the appearance of an abnormal $\chi(T)$ behaviour with the occurrence of a shoulder near $T_C = 265$ K, the Curie temperature of the ferromagnet Fe_2P . Figure 10 shows the Arrhenius plot of the electronic conductivity, σ_{elec} , of three LiFePO_4 samples: a pure material, a Fe_2P -containing sample, and a C-LFP. It is obvious that addition of either iron phosphide or carbon enhances greatly σ_{elec} but to the detriment of the capacity for the former compound, as it will be discussed next.

Figure 11 displays the electrochemical charge-discharge profiles of Li//LFP cells cycled at room temperature with pure LiFePO_4 and with Fe_2P -containing electrode material. It is obvious that at the rate 2C, the capacity retention decreases significantly for the material containing few % of Fe_2P . A close examination was made for the detection of any iron dissolution that could occur after long-term cycling. The analysis of iron species was investigated at the separator/lithium (SL) interface by SEM cross-section (slice view) as shown in Fig. 12a, b. The micrograph (Fig. 12a)

Fig. 10 Electronic conductivity of LiFePO_4 samples: pure material, Fe_2P -containing sample, and carbon-coated LiFePO_4

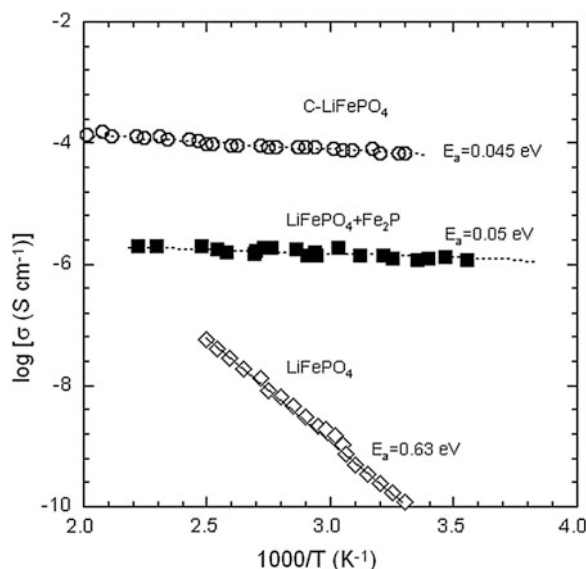
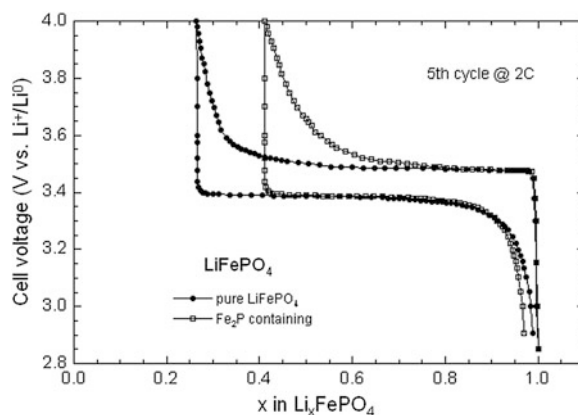


Fig. 11 Electrochemical charge-discharge profiles of $\text{Li}/\text{LiFePO}_4$ cells cycled at room temperature with pure LiFePO_4 and with Fe_2P -containing electrode material



obtained from evaluation of the earlier generation material shows the presence of iron islands at the SL interface. Obviously, some iron particles (or ions) migrate through the electrolyte from the LiFePO_4 positive electrode to the lithium negative. The net effect of this migration is a large decrease in capacity retention of the Li/LFP cell. Figure 12b shows the post-mortem micrograph obtained from tests with an optimised electrode in a Li cell with a lithium foil negative. In this case, there is no iron detected at the SL interface, which remained intact after 100 cycles. In fact, this high performance was possible not only because of the optimised synthesis of the LFP powders, but also because of strict control of the structural quality of the materials. Several physical methods were used to analyse the local structure and the electronic properties of the phospho-olivine framework [18].

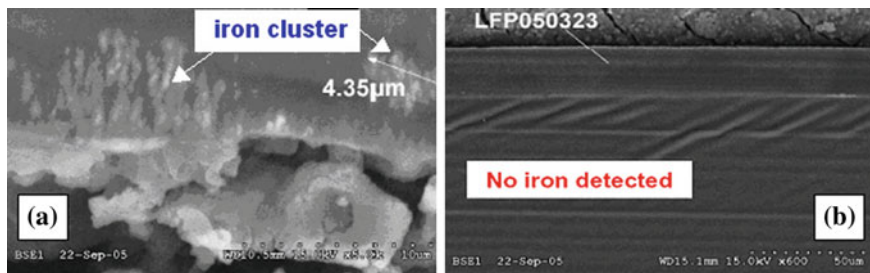


Fig. 12 Post-mortem SEM images of the detection of iron species at the separator/lithium interface. **a** Formation of iron islands at the interface with an earlier generation of LiFePO_4 . **b** No iron was detected at the surface of Li foil with the optimized LiFePO_4

3.7 Carbon Coating

To increase the electronic conductivity, it is a common practice in the production of Li-ion battery electrodes, to add carbon, either by use of carbon additives to the LiFePO_4 matrix [3], or by surface coating of LFP particles with thin layers of carbon [5, 6]. A seven-order-of-magnitude increase in the electronic conductivity has been reached by adding sucrose to produce carbon in LFP raw materials by a spray pyrolysis technique [7]. The addition of carbon has then the advantage of combining much better electronic conductivity, and high capacity. In particular, a capacity of about 160 mAh g^{-1} has been found for LFP coated with 1 wt% carbon [61]. Ravet et al. [5, 6] reported two ways to coat carbon: (i) mixing LFP powder with sugar solution and heating the mixture at 700°C , and (ii) synthesizing LFP with some organic materials added before heating. Although the way to add carbon is not fully optimized yet, the approach that consists in adding a carbon source at the beginning of the synthesis is more promising [6]. Recently, Julien et al. [33] demonstrated that better performance was obtained at high-rate discharge (3C) with 6 % carbon additive in the LFP electrode. This material is suitable for HEV application. This is consistent with the HRTEM images in Fig. 13, showing that the carbon coats the secondary particles with a typical radius of 100 nm and does not penetrate into the LFP particles [23].

3.8 Aging of LFP Particles Exposed to Water

It has been well-known for decades that all the lithium-ion batteries need to be protected against humidity. The main reason is that lithium is very reactive with water according to the chemical reaction $\text{Li} + \text{H}_2\text{O} \rightarrow \text{LiOH} + \frac{1}{2}\text{H}_2$. Lithium hydroxide (LiOH) is a corrosive alkali hydroxide. When crystallized, it is a white hygroscopic material. It is also soluble in water, a property that has been used to investigate aqueous lithium hydroxide as a potential electrolyte in Li-ion batteries

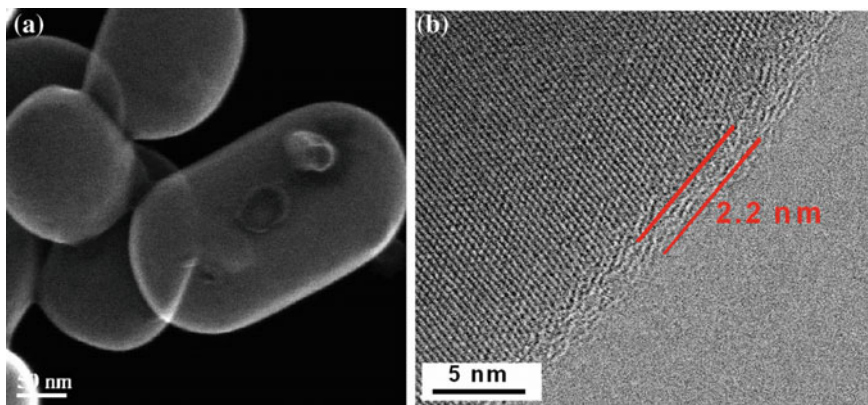
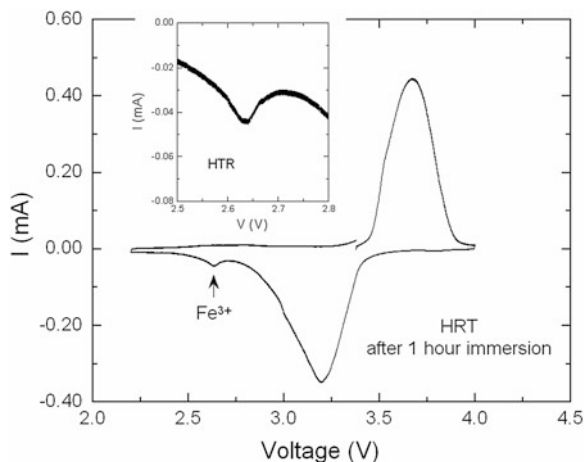


Fig. 13 HRTEM of carbon-coated LFP particles synthesized by hydrothermal method. The carbon coating, ~ 2 -nm thick was realized using the lactose route

with a LiFePO_4 cathode. Since the carbon coat is not a barrier for Li^+ -ion transport (the reason for the success of C-LiFePO_4 as a cathode element of Li-ion batteries), we expect the reaction with water to be effective, implying extraction of Li from LFP grains to interact with water. This delithiation is the only effect that is observed after exposure to H_2O in air, since the surface layer of the particles is also affected [63, 64]. Despite this reaction of lithium with humidity, a drop of LiFePO_4 particles into water was used in the laboratory to check the carbon-coating process by separating coated and uncoated particles. This means of characterization is based on the fact that when the C-LiFePO_4 powder is dropped into water, part of the carbon that links the particles unties and floats to the surface, retaining with it some of the particles, while the major part sinks. More recently, Porcher et al. [64] have determined that the exposure of C-LiFePO_4 particles to water results in the formation of a thin layer of Li_3PO_4 (few nm thick) at the surface of the particles as a result of migration of Fe into the water. In the present work, we investigate the effect of water on carbon-coated LiFePO_4 particles and analyze both the particles that have sunk and the floating part. We have shown that the water attacks the particles and that the carbon coat is not a protection because it detaches and is not waterproof [63]. We find that Fe is not the only element that reacts with the water, as the water contains also P and Li species after immersion of the LiFePO_4 . A strong interaction between LiFePO_4 with H_2O molecules was not necessarily expected. Since iron phosphate is hydrophobic, the surface layer protects the iron against oxidation and corrosion. Intuition would then have suggested that, upon immersion of LiFePO_4 in water, a delithiation in a thin layer at the surface would lead to the formation of a FePO_4 layer that would protect the particles against any other damage. Quantification of magnetic analysis of LFP grains shows that the thickness of the delithiated surface layer is ~ 3 nm.

The cyclic voltammograms of LFP powders after immersion for 1 h in water are reported in Fig. 14. In these measurements, an initial 3.2 V working potential is

Fig. 14 Electrochemical performance of the C-LiFePO₄ synthesized by hydrothermal method in LiPF₆-EC-DEC/Li cells at room temperature. Cathode particles were immersed in water for 1 h, then dried for 48 h at 85 °C



applied. Then, the voltage was varied at the rate 1.25 mV per minute, as shown in the figure: a voltage increase up to 4 V is followed by a decrease to 2.2 V and an increase again up to 3.2 V. Besides the peak associated with Fe²⁺, the part of the curve obtained by decreasing the voltage shows a secondary peak at 2.63 V that is characteristic of the Fe³⁺ in iron oxide (vs. more than 3.5 V in phosphate) [32]. The presence of Fe³⁺ ions in LFP samples confirms the delithiation of the surface layer evident in the previous sections. On the other hand, upon increasing the voltage again, this signal disappeared, which shows that the voltammogram before exposure to H₂O was recovered. Therefore, the surface layer was lithiated again during Li insertion, and the effect of immersion in water was reversed [63]. Note, however, that this recovery could be obtained because we were dealing with a half-cell, i.e. with lithium metal as an anode. In this case, the lithium anode acts as a reservoir of lithium. In a full cell where the negative electrode would be carbon or Si or any metal oxide, however, one would not such a reservoir so that no recovery would have been obtained, so that, in practice, it is important to keep the LFP powder dry.

The same effect holds true for longer immersion times of a few days. In the following experiments, the samples were immersed for 63 h. Then, the samples were dried for 48 h at 85 °C. Moreover, it should be noted that the open-circuit voltage (OCV) decreased by 2.3 % on immersion in water. Since the OCV is directly related to the state of charge of the battery, it can be viewed as an indirect measurement of the delithiation rate of the battery. Indeed, this result is fully consistent with the 4 % delithiation rate deduced from the magnetization measurements, and the 1–3 % loss of Fe and P in the immersion process estimated from the physical and chemical analyses. It thus fully confirms that the delithiation process is located in the surface layer. The effect of H₂O on the electrochemical properties was also evaluated by exposure of the sample to ambient air. This effect is illustrated for a hydrothermal sample in Fig. 15, which shows the change of the capacity as a function of time at different temperatures in dry atmosphere and in ambient air (55 % relative humidity) [63].

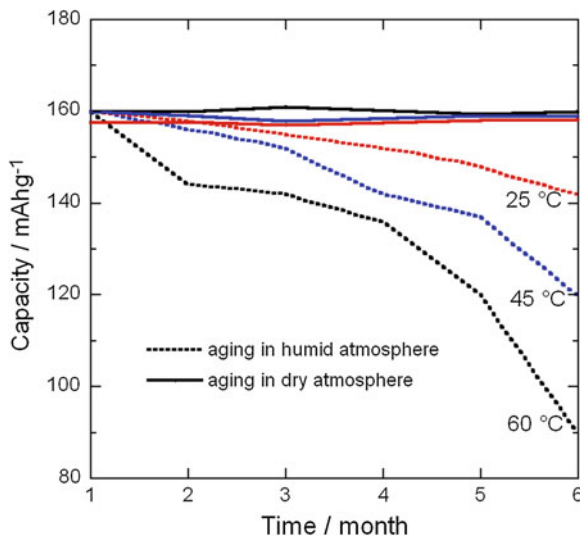
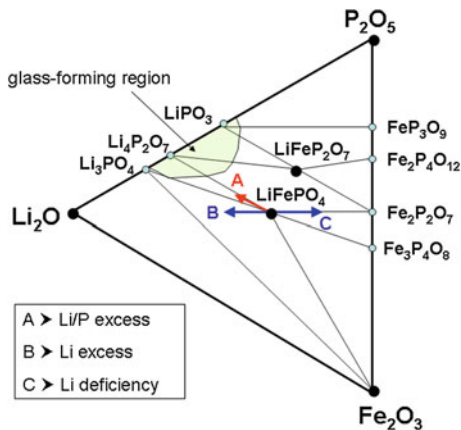


Fig. 15 Capacity of the C-LiFePO₄/LiPF₆-EC-DEC/Li cells as a function of time spent in dry atmosphere and in ambient atmosphere (55 % relative humidity), at three different temperatures. The temperatures at which the full lines (in dry atmosphere) have been obtained can be distinguished by the fact that they do not overlap, and the higher capacity is obtained at lower temperature

3.9 Non-stoichiometric LFP: Defects and Related Properties

Deviation from ideal stoichiometry of LiFePO₄ has been investigated [62]. Any attempt to increase the Li concentration of samples prepared either by the precursor precipitation route or the continuous aqueous precursor synthesis route results in the formation of lithium phosphate impurity, in addition of stoichiometric LFP free of any Li vacancy. On another hand, Li-deficient homogenous solid solutions of composition Li_{1-2x}Fe_xFePO₄ could be obtained (Fig. 16). For $x \geq 0.06$, however, a sarcopside impurity phase is formed. Investigations of structural properties allowed us to define the defect responsible for the solid solution as $\text{Fe}_{\text{Li}}^{\bullet} + \text{V}_{\text{Li}}'$ in the Kroger-Vink notation. Since the chemical formula of the sarcopside is obtained by writing $x = 1/2$ in the chemical formula of the solid solution, this impurity phase can be viewed as a condensation of the $\text{Fe}_{\text{Li}}^{\bullet} + \text{V}_{\text{Li}}'$ defects. Magnetic measurements showed that isolated lithium vacancies V_{Li}' are also diluted in the Li_{1-2x}Fe_xFePO₄ matrix. The negative charge of the isolated V_{Li}' is compensated by the valence change $\text{Fe}^{2+} \rightarrow \text{Fe}^{3+}$ of an iron ion in its vicinity, forming a small magnetic polaron that is detected by magnetic measurements. The concentration of such polarons, however, remains very small as it saturates to a concentration of 0.2–0.3 mol%, much smaller than the concentration x in V_{Li}' bound to $\text{Fe}_{\text{Li}}^{\bullet}$. The electrochemical features are significantly damaged by the $\text{Fe}_{\text{Li}}^{\bullet}$ defects that block the diffusion of lithium along the corresponding channel, while the Li₃PO₄ only acts as an inert mass. Defects

Fig. 16 Ternary phase diagram of off-stoichiometric LiFePO_4 . The composition moves toward three directions such as *A* for Li/P excess, *B* for Li excess only and *C* for Li deficient



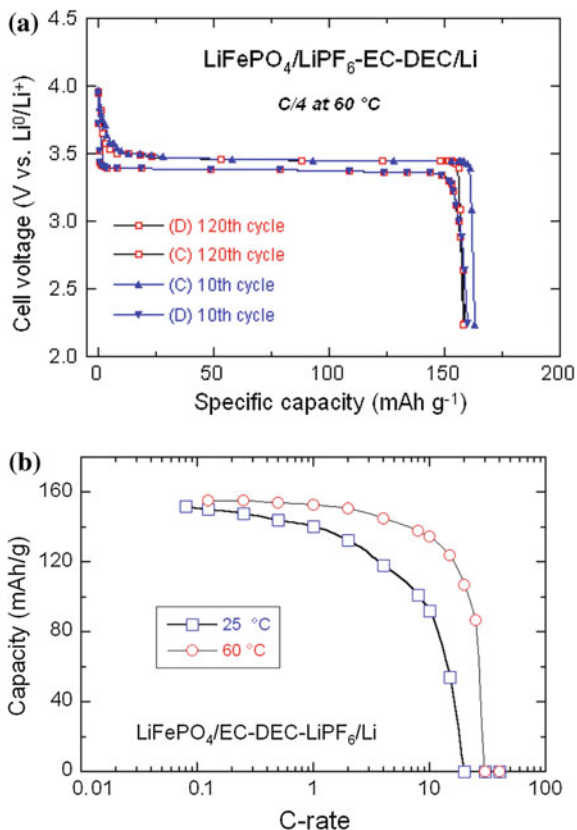
have an important impact on the electrochemical properties. The study of small particles (40 nm) has shown that the presence of defects or structural disorder favors the formation of the solid solution Li_xFePO_4 in the lithiation/delithiation process, instead of the phase separation between a Li-rich and Li-poor phase. This phenomenon has been observed in the surface layer (3 nm thick) alone in case the core of the particles is free of defects and well crystallized. It has also been observed in the whole volume of the particle when not only the surface layer, but the total particle is full of defects and cation vacancies, while the classical separation in two phases is recovered in case the particles (core plus surface layer) are free of defects.

3.10 Electrochemical Performance of LFP

Here, we present an overview of the high-temperature performance for an optimized LiFePO_4 sample, i.e. carbon-coated (C-LFP). The coffee-bag cell was charged and discharged at $C/8$ for the first cycle followed by 12 cycles at $C/4$ with 1 h rest before each charge and discharge. This high-temperature test was made at 60°C , which is the appropriate condition to investigate possible iron dissolution in non-aqueous electrolytes [18, 65]. From structural and elemental analysis, no iron, even at the ppm level, was found in the electrolyte solution. Thus, all these data converge to the conclusion that the optimized LiFePO_4 is not soluble at 60°C .

The typical electrochemical profile of the C-LFP/1 mol. L^{-1} LiPF_6 -EC-DEC/Li 18,650-type cell cycled at 60°C is shown in Fig. 17a. These experimental conditions (ca. 60°C) have a severe impact on the kinetics of the $\text{Fe}^{2+}/\text{Fe}^{3+}$ redox reaction, but the recent report from Hydro-Québec Research Labs showed that this type of C-LFP electrode can be cycled at 60°C without significant capacity loss for over 200 cycles [35]. Optimized particle size in the range 200–300 nm agrees well with the average diameter of grains L that validates Eq. (2) with $D^* \approx 10^{-14} \text{ cm}^2 \text{ s}^{-1}$

Fig. 17 **a** Voltage-capacity cycle for Li//LFP 18,650-type cell cycled at C/4 rate at 60 °C. **b** Peukert plots of the C-LiFePO₄/LiPF₆-EC-DEC/Li cells as a function of the working temperature 25 and 60 °C



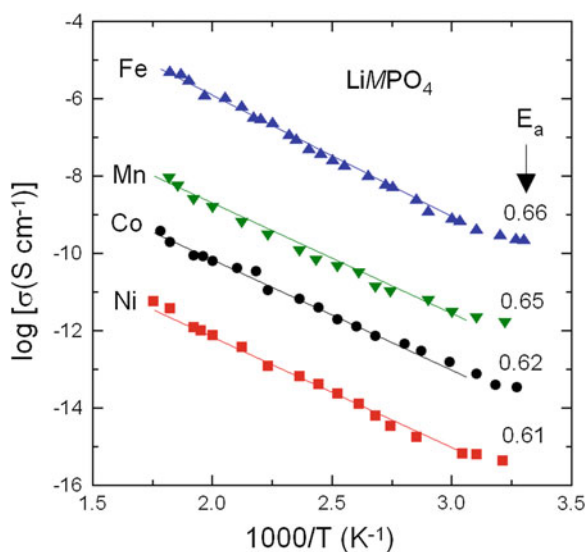
in the LiFePO₄ matrix. The 10th and 120th cycle shows a similar specific capacity of 160 mAh g⁻¹. These results illustrate the excellent electrochemical performance of the carbon-coated olivine material. The electrode can be fully charged up to 4 V, which is its most reactive state. This remarkable performance is attributed to the optimized carbon-coated particles and their structural integrity under a large current in the electrode. Even at such a high cycling rate, C-LiFePO₄ exhibits rapid kinetics of lithium extraction and it realizes most of its theoretical capacity (170 mAh g⁻¹). The discharge profile appears with the typical voltage plateau (at ca. 3.45 V vs. Li⁰/Li⁺) attributed to the two-phase reaction of the (1 - x) FePO₄+xLiFePO₄ system. The modified Peukert plots of cell cycled at 25 and 60 °C are shown in Fig. 17b. The cells were cycled in the potential range 2.5–4.0 V. The discharge capacity and electrochemical utilisation, i.e. the ratio discharge/charge versus cycle number is excellent for the C-LiFePO₄/Li cells. At 10C rate, these Li-ion cells provide coulombic efficiencies 85 % at 60 °C.

4 Lithium Manganese Olivine

LiMnPO_4 (LMP) is an attractive cathode material that offers several advantages: (i) it is low cost, (ii) due to the $\text{Mn}^{2+}/\text{Mn}^{3+}$ redox potential of 4.1 V versus Li^0/Li^+ it presents higher voltage than LFP and (iii) it is suitable for the electrolytes used in Li batteries. However, the intrinsically specific capacity is restrained by (i) the inherently low ionic and electrical conductivities of LiMnPO_4 that seriously limit Li^+ insertion and extraction and (ii) the high kinetic barrier at the mismatched interface of $\text{MnPO}_4/\text{LiMnPO}_4$ due to the severe Jahn-Teller (JT) distortion [66]. As shown in Fig. 18, the electrical conductivity of LiMnPO_4 is lower than the already insulating LiFePO_4 by 5 orders of magnitude [67] making it challenging to achieve high capacity at high rates for LiMnPO_4 using methodologies developed for LiFePO_4 . LiMnPO_4 crystallizes in an ordered olivine structure indexed by orthorhombic $Pnmb$ space group. Typical crystallographic parameters are $a = 6.106(1) \text{ \AA}$, $b = 10.452(1) \text{ \AA}$, and $c = 4.746(1) \text{ \AA}$.

LMP was prepared by the same methods described before for other olivine frameworks [68–92]. Figure 19 presents the HRTEM images of LMP samples with different morphologies. Synthesis techniques include solid-state reaction with different carbon sources [91], precipitation method using different precursors such as $\text{NH}_4\text{MnPO}_4 \cdot \text{H}_2\text{O}$, $\text{MnPO}_4 \cdot \text{H}_2\text{O}$ [68, 95], and modified ionothermal synthesis [69]. Drezen et al. [68] prepared LMP with different crystallite sizes by varying the sintering temperature. Using the polyol route, Wang et al. [69] and Martha et al. [70] obtained carbon-coated LMP particles of 30 nm that delivered a specific capacity of 110 mAh g^{-1} at 1C rate. A flower-like $\text{LiMnPO}_4\text{-C}$ composite prepared by solid-state reaction showed a reversible capacity of 85 mAh g^{-1} at a rate of

Fig. 18 The electrical conductivity of LiMPO_4 ($\text{M}=\text{Fe, Ni, Co, Mn}$) olivine materials. Numbers indicate the activation energy in eV. The low conductivity is related to the small free volume and separation of MO_6 octahedra by oxygen atoms of the $(\text{PO}_4)^{-3}$ anions



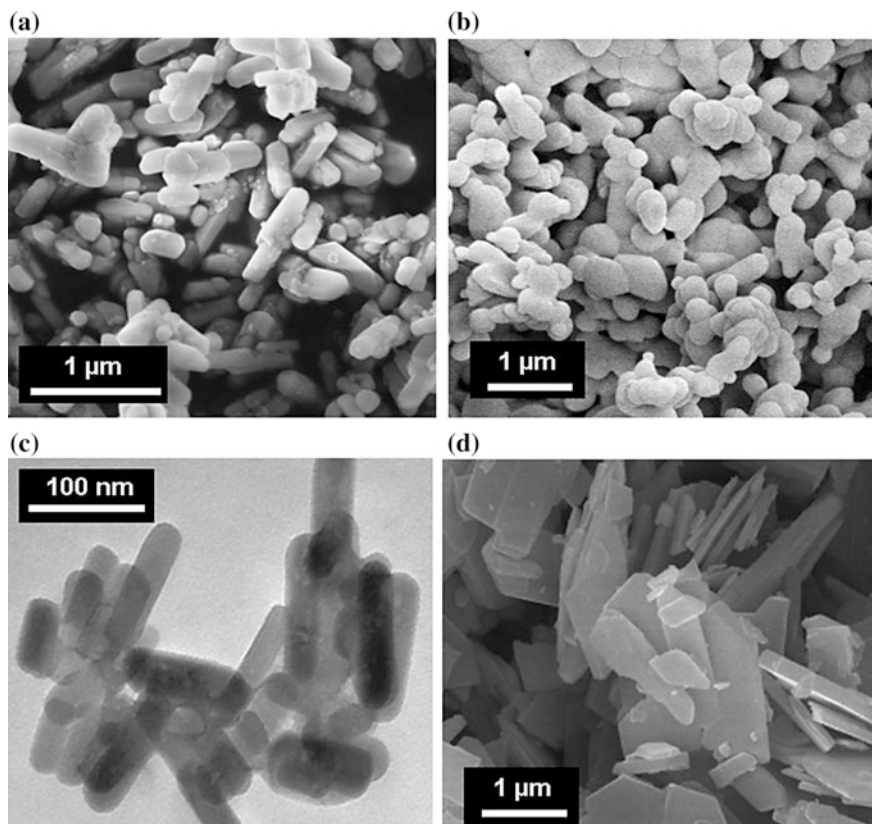
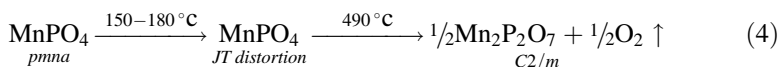


Fig. 19 HRTEM images of LMP samples with different morphologies. LMP nanoparticles were prepared by (a) hydro-thermal method with ascorbic acid, b polyol reflux method with tetraethylene glycol as solvent, c thermal decomposition method using oleic acid as surfactant and benzyl ether as solvent, and d precipitation route

0.05C [71]. The solution-based synthetic routes such as spray pyrolysis [72, 73], precipitation, sol-gel [74], hydrothermal method [75], solvothermal route [76, 77] and polyol synthesis [78] provide nanostructured LMP powders with enhanced electrochemical properties, which is mostly attributed to the higher chemical homogeneity and narrow particle size distribution of the material. The best results were obtained for LiMnPO_4 prepared via sol-gel, hydrothermal and co-precipitation routes. However, these techniques use the very low concentration of starting materials, which leads to the very low production rate [79]. 5–10 nm thin rod shaped LMP nanoparticles were synthesized by an improved thermal decomposition method using oleic acid as surfactant and benzyl ether as solvent [80]. LMP nanorods were also synthesized by modified polyol and resin coating processes to enhance their conductivity as well as their electrochemical properties with a capacity up to 120 mAh g^{-1} at 1C rate [81]. $\text{LiCu}_x\text{Mn}_{1-x}\text{PO}_4/\text{C}$ nanorods prepared

by a simple solvothermal process followed by calcination show that Cu successfully entered into the lattice of LiMnPO_4 and induced a decrease in the lattice parameters; however, a small initial discharge capacity of 87.5 mAh g^{-1} at $0.5C$ was reported [82]. A microwave irradiated solvothermal method with tetraethylene glycol as solvent was used to prepare dimensionally modulated, single-crystalline LiMnPO_4 with nano-thumblike shapes for high-power applications [94]. A two-step procedure for preparation of LMP with small particle size (15–20 nm) and embedded in a carbon matrix was presented by Pivko et al. [83]. Despite the nanosized particles limited capacity of 130 mAh g^{-1} at $C/20$ rate was observed at 55°C after 100 cycles. A sequential precipitation method was applied to LiMnPO_4 olivine by confining $\text{Mn}_3(\text{PO}_4)_2$ precipitation on surface of a precursor seed of Li_3PO_4 that results in discharge capacity of 62 mAh g^{-1} at $5C$ rate for the size of LMP particles limited to less than 100 nm [84].

Kim et al. [85] claim to improve significantly the electrochemical properties of LMP by small amounts of co-doping of Fe and Co. The 4.0 V redox potential is achieved, while the kinetics are enhanced through formation of a local solid-solution like phase in the matrix, which is expected to lower the nucleation barrier of the delithiated phase and reduced the JT distortion. Lee et al. [86] evidenced the intercrystallite ionic transport in $40 \text{ nm} \times 200 \text{ nm}$ sized LiMnPO_4 nanorods synthesized by the modified polyol method that resolves the problem of particle inhomogeneity occurring in stoichiometric synthesis. LMP nanoplates with thickness of 50 nm grew in the (100) plane via solid-state reaction in molten hydrocarbon such as paraffin and delivered a capacity 130 mAh g^{-1} at $C/10$ rate [87]. The effect of different carbon sources on the electrochemical properties of rod-like LMP/C nanocomposites was reported by Li et al. [88]. A reversible capacity of $\sim 153 \text{ mAh g}^{-1}$ at a rate of $C/10$ was obtained with beta-cyclodextrin as the carbon source, which is much better than that obtained from ascorbic acid, citric acid, glucose and sucrose. A carbon matrix, for restricting growth of LMP crystallites, was built on the small Li_3PO_4 crystallites precipitated from aqueous solutions, by the pyrolysis of sucrose. Small crystallite-size (8–12 nm) particles were successfully prepared using the carbon coated Li_3PO_4 as one of the reactants (the other reactant is MnSO_4) and the nuclei by a solvothermal method [89]. Chen and Richardson [90] demonstrated that the release of oxygen from LMP material occurs at 150°C followed by the combustion of the electrolyte at 215°C for a total heat of 884 J g^{-1} that is less thermal stability than LFP. The thermal stability mechanism on charged LMP electrode can be expressed as:



From in-situ XRD, XPS and EDAX results on the charged and discharged LMP cathode, the charged state of MnPO_4 undergoes structural changes due to Jahn-Teller effect at above 180°C and followed by reduction into pyrophosphate $\text{Mn}_2\text{P}_2\text{O}_7$ at ca. 490°C . TGA-DSC measurements shown that the weight loss up to 450°C for charged MnPO_4 shows similar behavior as that of discharged LiMnPO_4

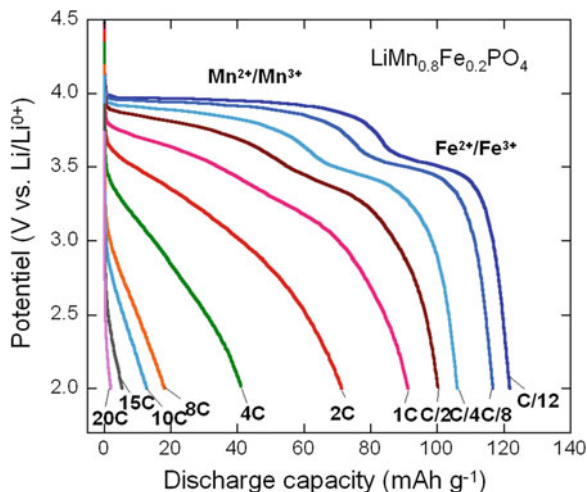
cathode, indicating that the reaction is a decomposition of the SEI layer formed during high-voltage electrochemical cycling process. Note that a sharp exothermic peak is observed in the DSC scan during reduction due to the oxygen and CO₂ gas released after reacting with conductive carbon additive.

5 Lithium Mn–Fe Olivine

The solid solution LiMn_yFe_{1-y}PO₄ (LMFP) looks promising because it operates at 3.4–4.1 V that is not so high as to decompose the organic electrolyte but not so low as to sacrifice energy density [95–101]. Gardiner and Islam [99] have discussed the formation of the intrinsic defect-type with the lowest energy in the cation anti-site defect, in which Li and Fe/Mn ions exchange position in 4c sites. Migrations energies for Fe and Mn anti-site cations on Li sites suggest that Mn defects would impede bulk Li mobility in LiMnPO₄ to a greater extent than Fe anti-site defects in LiFePO₄. The electrochemical properties of the LMFP materials prepared by chelating-assisted hydrothermal method have been investigated by a number of research groups (see [100] and references herein). Trottier et al. [100] investigated the electrochemical properties of LiMn_yFe_{1-y}PO₄ (0.5 ≤ y ≤ 0.8) mixed-metal phospho-olivines (LMFP) grown by hydrothermal route assisted by ascorbic acid as chelating agent. Hong et al. [94] synthesized LiMn_{1-x}Fe_xPO₄ by a facile solvo-thermal approach with an excess of 20 wt% sucrose to yield carbon coating. Kosova et al. [95] reported structural studies of nanosized LiFe_{0.5}Mn_{0.5}PO₄ prepared by mechanochemically assisted carbothermal reduction route under cycling by in situ synchrotron diffraction. Wang et al. [96] reported the synthesis of LiMn_{1-x}Fe_xPO₄ nanorods on reduced graphene oxide sheets.

The rate capability for Li/C–LiMn_{0.8}Fe_{0.2}PO₄ cell is shown in Fig. 20. The cell was charged and discharged at the same C-rate starting from C/12 to 20C. For instance, the composite electrode including C–LiMn_{0.8}Fe_{0.2}PO₄ electrode 5 wt% Denka and 5 wt% VGCF delivers a capacity 92 mAh g⁻¹ at 1C rate. For LiMn_{0.8}Fe_{0.2}PO₄, the electrode exhibited two reversible discharge plateaus at 3.95 and 3.52 V versus Li⁰/Li⁺ related to the Mn³⁺/Mn²⁺ and Fe³⁺/Fe²⁺ redox couples, respectively. From these profile, several conclusions can be drawn: (i) the charge-discharge profile exhibits similar shape for all compositions, (ii) the two pairs of peaks in dx/dV curves shift slightly with y as a result of the inductive effect (charge: 3.54 and 4.12 V; discharge 3.95 and 3.47 V for y = 0.6), (iii) the potentials of the reduction peaks are more sensitive than those of the oxidation peaks to the Mn²⁺-substitution, (iv) a small increase of the over-voltage is seen as a function of y, and (v) the highest specific capacity is 130 mAh g⁻¹ for y = 0.5, when the electrode was kept at 4.5 V until C/50 rate. Note that the polarization potential increases slightly for the Mn-rich compounds, which we attribute to a Jahn-Teller effect increased by the alloying process, rather than the formation of the intrinsic defect-type with the lowest energy in the cation anti-site defect, in which Li and Fe/Mn ions exchange positions.

Fig. 20 Typical discharge curves of the Li//LiMn_yFe_{1-y}PO₄ ($y = 0.8$) cell



Magnetic properties of the solid solution LiMn_yFe_{1-y}PO₄ showed that for $y \leq 0.6$, all the Mn³⁺ ions in delithiated LMFP are in the high-spin state ($S = 2$). At larger manganese concentration, however, the Mn³⁺ ions in excess of the critical concentration $y_c = 0.6$ undergo a transition to the low-spin state ($S = 1$). The spin-transition of Mn³⁺ in concentration ($y - y_c$) to the low-spin state is at the origin of the strain fields at the molecular scale that increase with y for $y > 0.6$, and ultimately prevents the full delithiation for $y > 0.8$. This result sheds light on the reason for the degradation of cathode properties in Mn-rich compounds of the heterosite–purpurite series, while the electrochemical properties are good in the range $y \leq 0.6$ but only at slow rates, due to the very small hopping mobility of the small polaron [97, 98]. It is obvious that LMP exhibits inferior electrochemical performance compared with LFP. Optimizing the synthesis process and carbon coating should lead to promising electrochemical properties for LMP nanoparticles.

6 Lithium Cobalt Phosphate

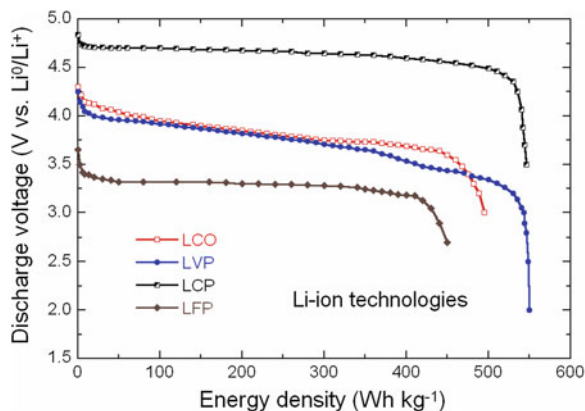
Lithium cobalt phosphate, LiCoPO₄ (LCP) has attracted attention since it offers both flat high potential (at approximately 4.8 V vs. Li⁰/Li⁺), good theoretical capacity (167 mA g⁻¹) and smaller structure volume change. As other olivine compounds, LCP crystallizes with the orthorhombic symmetry (*Pnma* S.G.) with lattice parameters: $a = 10.2048$ Å, $b = 5.9245$ Å, and $c = 4.7030$ Å. However, like in the case of LiMnPO₄, the electrochemical performance of pristine LCP is very poor due to the low intrinsic electronic and ionic conductivity [67, 102–116]. Zhao et al. [116] prepared LCP micro-rods with the diameter of ca. 500 nm and length of ca. 5 μm by a hydrothermal method, which delivered a discharge capacity of only

65 mAh g⁻¹ at C/10 rate. Solution-based methods are appealing to control LCP particles size, shape and morphology of nanocrystals. Truong et al. [102] used the supercritical fluid (SCF) processing with different amines having long alkyl chain such as hexamethylene diamine for adjusting physicochemical properties. Hedgehog-like LCP with hierarchical microstructures was first synthesized via a simple solvothermal process in water–benzyl alcohol mixed solvent at 200 °C [103]. The hedgehog-like microstructures in the size of about 5–8 μm were composed of large numbers of nanorods in diameter of ca. 40 nm and length of ca. 1 μm, which are coated with a carbon layer of ca. 8 nm in thickness by in situ carbonization of glucose during the solvothermal reaction. As a 5 V positive electrode material for rechargeable lithium battery, the hedgehog-like LiCoPO₄ delivered an initial discharge capacity of 136 mAh g⁻¹ at C/10 rate and retained its 91 % after 50 cycles. LCP nanocrystals with (010) orientation were prepared by solvothermal method employing ethanol as the solvent and poly(vinyl pyrrolidone) as the carbon source and template [104].

In the early work by Amine et al. [117], it is demonstrated that Li can be reversibly removed from LCP at an average voltage of 4.8 V versus Li⁺/Li with only a small contraction in the unit cell volume of the olivine lattice and the formation of a second olivine-like phase upon Li extraction from Li_xCoPO₄ with limited Δx = 0.42 lithium per formula unit. The electrochemical properties of LiCoPO₄ have been studied as a function of synthesis parameters. Effects on the discharge capacity have been investigated and capability improvements include: mixing LNP–LCP to obtained solid solutions as cathodes [105], carbon coating [106, 107], effect of oxygen partial pressure on the discharge capacity [108]. Wolfenstine et al. [109] have studied the structural evolution of LiCoPO₄ delithiated by the chemical oxidation. Okada et al. [110] have shown that LiCoPO₄ exhibited the highest 4.8 V discharge plateau of 100 mAh g⁻¹ after initial charging to 5.1 V giving an energy density of 480 Wh kg⁻¹ comparable to that of LiCoO₂. Electrical conductivity of LCP and mixed (Co, Ni), (Co, Mn) compounds [111], and of doped LCP [112] have also been explored. LCP having low electron conductivity, its use as the cathodic material is possible only in the case of synthesis of the LiCoPO₄/C composite [103]. Such composites can be discharged at the potentials of 4.7–4.8 V. However, cyclability of such composites is very low, as decomposition of liquid electrolyte occurs under charging in the potential range of 4.8–5.1 V simultaneously with oxidation of Co²⁺ to Co³⁺. The initial discharge capacity of LiCoPO₄/C is close to the theoretical one that is about 167 mAh g⁻¹. Figure 21 compares the discharge curves of various lithium cells including LiCoPO₄ (LCP), LiCoO₂ (LCO), LiFePO₄ (LFP) and Li₃V₂(PO₄)₃ (LVP).

The phase transitions occurring upon lithium insertion-extraction of LiCoPO₄ have been investigated by several groups [111–115]. A two phase mechanism was confirmed by in situ synchrotron diffraction [111]. An amorphization of the phosphate was observed after electrochemical or chemical oxidation [113]. Nagayama et al. [114] suggested from X-ray absorption spectroscopy a hybridization effect between the Co 3d and O 2p orbitals and the polarization effect introduced by Li ions. Bramnik et al. [115] revealed the appearance of two

Fig. 21 Comparison of discharge curve of several cathode materials: LiCoPO_4 (LCP), LiCoO_2 (LCO), LiFePO_4 (LFP) and $\text{Li}_3\text{V}_2(\text{PO}_4)_3$ (LVP)



orthorhombic phases upon electrochemical Li extraction. The LiCoPO_4 and the Li deficient phases, $\text{Li}_{0.7}\text{CoPO}_4$ and CoPO_4 , are responsible for the two voltage plateaus at 4.8 and 4.9 V versus Li^+/Li . The hedgehog-like LiCoPO_4 microstructures in the size of about 5–8 μm are composed of large numbers of nanorods in diameter of ca. 40 nm and length of ca. 1 μm , which are coated with a carbon layer of ca. 8 nm in thickness by in situ carbonization of glucose during the solvothermal reaction. As a 5 V positive electrode material for rechargeable lithium battery, the hedgehog-like LiCoPO_4 delivers an initial discharge capacity of 136 mAh g^{-1} at C/10 rate and retains its 91 % after 50 cycles [111]. Surface modification of LCP particles results in a satisfactory cyclability for LiCoPO_4 to be used as a 5 V cathode material [115]. The capacity retention of Al_2O_3 -coated LCP was 105 mAh g^{-1} after 50 cycles at $T = 55^\circ\text{C}$. Jang et al. [118] claimed that LiFePO_4 coated LCP particles prepared by SSR method (~ 100 – 150 nm) show improved battery performance with an initial discharge capacity of 132 mAh g^{-1} , but did neither mention the C-rate nor the current density. The ability to suppress thermal runaway of LiMPO_4 olivine frameworks is attributed to the high covalent feature of the P–O bonds in the tetrahedral (PO_4) units, which stabilizes the olivine structure and prevents oxygen release from the charged (delithiated) olivine materials up to 600 $^\circ\text{C}$. This is still controversial in LCP and LNP olivine lattices. In particular, a thermal instability has been reported in the charged (i.e. delithiated) state of LiCoPO_4 [119]. Both olivine-like phases Li_zCoPO_4 ($z = 0.6$) and CoPO_4 appearing during the delithiation of LiCoPO_4 are unstable upon heating, and decompose readily in the range 100–200 $^\circ\text{C}$. The decomposition of lithium-poor phases leads to gas evolution and the crystallization of $\text{Co}_2\text{P}_2\text{O}_7$. Incorporation of lithium bis(oxalato)borate (LiBOB) as additive in conventional electrolyte solutions enhances the electrochemical performance of LCP electrode [120].

7 Lithium Nickel Phosphate

Compared with LiFePO_4 and LiMnPO_4 , LiNiPO_4 (LNP) displays much higher redox potential [121–143]. Wolfenstine and Allen [121] determined the $\text{Ni}^{3+}/\text{Ni}^{2+}$ redox potential between 5.1 and 5.3 V for the LNP olivine lattice. To overcome the problems with low electrolyte stability, a 1 mol L^{-1} LiPF_6 in tetramethylene sulfone electrolyte was used because of its high oxidative stability, around 5.8 V versus Li^0/Li^+ . These experimental values are in excellent agreement with the theoretical predictions [139–141]. Recently, a review has presented the progress in the fabrication of LNP powders and the general synthesis approaches to circumvent the drawbacks of LNP [142]. Among the various synthesis approaches, solution-based methods have been successful for LNP. Standard hydrothermal route starts with mixing Li salt with either $\text{Ni}(\text{C}_2\text{H}_3\text{O}_2)_2 \cdot 4\text{H}_2\text{O}$ or $\text{Ni}(\text{NO}_3)_2 \cdot 6\text{H}_2\text{O}$ in different reaction media such as NH_4OH , cotton fibers, 1,2-propanediol and ethylene glycol [36, 143–152]. Tsai [145] produced LiNiPO_4 nanocrystals via a microemulsions method and determined that the water-to-surfactant ratio directly affects the particle size and shape. Various attempts were made to prepare nanosized LNP particles using sol-gel method. Prabu and Selvasekarapandian [146] prepared plate-like LNP (surface area $0.25 \text{ m}^2 \text{ g}^{-1}$) by adding citric acid and polyethylene glycol as chelating agent for gelation. Yang and Xu [144] obtained phase pure LiNiPO_4 with desirable particles sub-micron size and free of agglomeration. Nanometric crystallite size were obtained by using both the acrylamide and N,N' -methylenebis(acrylamide) as gelling agents [147]. Lanthanum- and zinc-doped LiNiPO_4 was prepared by the polyol method from metal acetates and 1,2 propanediol as polyol medium [121–122, 148]. Nano-particles <50 nm were obtained. Dimesso et al. [123] reported the synthesis of graphitic carbon foam— LiNiPO_4 composites prepared by a Pechini-assisted sol-gel method using water as solvent. The difficulties in obtaining a LNP pure phase have been pointed out by several groups [121, 123–125].

Solid-state reaction has been widely used for LNP production. Impurities such as NiO , Ni_3P , $\text{Ni}_2\text{P}_2\text{O}_7$ and $\text{Li}_2\text{Ni}_3(\text{P}_2\text{O}_7)_2$ have been identified. The carbothermal-reaction method was employed by Herle et al. [126] using heat-treatment in flowing argon atmosphere. The most commonly used precursors are Li_2CO_3 , $\text{LiOH} \cdot \text{H}_2\text{O}$, Li_3PO_4 , but also LiH_2PO_4 for Li, $\text{Ni}(\text{COO})_2 \cdot 2\text{H}_2\text{O}$, $\text{Ni}(\text{C}_2\text{H}_3\text{O}_2)_2 \cdot 4\text{H}_2\text{O}$, $\text{Ni}(\text{C}_2\text{H}_3\text{O}_2)_2$, NiO , $\text{Ni}(\text{CO}_3)$, $\text{Ni}(\text{OH})_2$, $\text{Ni}_3(\text{PO}_4)_2$ for Ni, and $\text{NH}_4\text{H}_2\text{PO}_4$, $(\text{NH}_4)_2\text{HPO}_4$, a mixture of $(\text{NH}_4)_2\text{HPO}_4$ and P_2O_5 or $(\text{NH}_4)_3\text{PO}_4$ for P, respectively. Sugiyama et al. [127] prepared phase pure LiNiPO_4 by planetary ball milling and calcination under argon at 750 °C for 6 h. Wang et al. [128] only obtain phase pure LiNiPO_4 after calcination above 800 °C, while lower temperature processes provide samples containing Li_3PO_4 and NiO_x . The olivine analogue compound containing mixed (Mg, Ni) cations contained Li_3PO_4 as a second phase upon synthesis; however a carbothermal reduction method produced a single-phase compound [129]. Solid-state methods are also of importance in terms of obtaining ordered crystal structure. As an example, Julien et al. [125, 130] reported the growth of LiNiPO_4 with high purity using modified solid-state reaction with different sets of reactants such as (i)

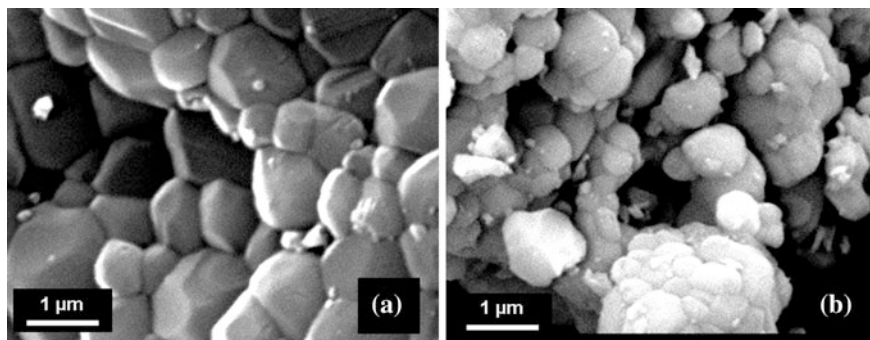


Fig. 22 SEM images of LiNiPO_4 samples synthesized by **a** the ammonium-hydrogen-phosphate route, and **b** the lithium-dihydrogen-phosphate route

Li_2CO_3 , $(\text{NH}_4)_2\text{HPO}_4$, and NiO (ammonium-hydrogen-phosphate route), and (ii) NiO and LiH_2PO_4 (lithium-dihydrogen-phosphate route) dissolved in acetone solution. Single phases of LNP were obtained after sintering at 800°C for 36 h. Figure 22 shows the typical SEM images of LNP powders synthesized by solid-state reactions [125]. Structural characteristics of particle synthesized by the ammonium-hydrogen-phosphate route were studied in detail using analytical electron microscopy. Results are shown in Fig. 23. The high-resolution transmission electron microscopy (HRTEM) and selected area electron diffraction (SAED) images indicate that the grown LiNiPO_4 is well-crystallized in the olivine structure without any indication of crystallographic defects such as dislocations or misfits.

The absence of redox peaks when LNP was heated under argon suggests that this material has a very low intrinsic electrical conductivity and hence, additional treatments such as carbon coating are required for LNP to exhibit Li insertion/deinsertion. Indeed, Rissouli et al. [67] determined that the electrical conductivity of LiNiPO_4 was 2–3 decades lower than that for LiCoPO_4 and LiMnPO_4 (Fig. 18). Such a poor electronic conductivity has been recently confirmed by ac measurements on nano-crystalline powders [131]. Herle et al. [126] have pointed out that LiNiPO_4 exhibits a percolating nano-network of metal-rich phosphides (i.e. Ni_3P , Ni_2P , or NiP_3) responsible for enhanced conductivity. Magnetic anisotropy in Li-phosphates and the origin of their magneto-electric properties have been investigated [125, 132, 133]. Magnetic properties of LCP and LNP show that antiferromagnetic $M\text{--O--}M$ superexchange interactions couple the spins closely in planes parallel to (100) [133] with a Néel temperature $T_N = 21\text{ K}$. The magnetically ordered phases and spin dynamics of magnetoelectric LiNiPO_4 have been studied in magnetic field as high as 17.3 T along the c axis and up to 16 T along the a - and b -axis [134]. Vaknin et al. reported the commensurate-incommensurate magnetic phase transition in magneto-electric single crystal LiNiPO_4 [135]. Local environment and bonding strength of cations were studied by vibrational spectroscopy, i.e. Raman and FTIR [125, 136].

The information available about the electrochemical performance of LNP is very limited. Few reports have shown that LNP is not electrochemically active when it is

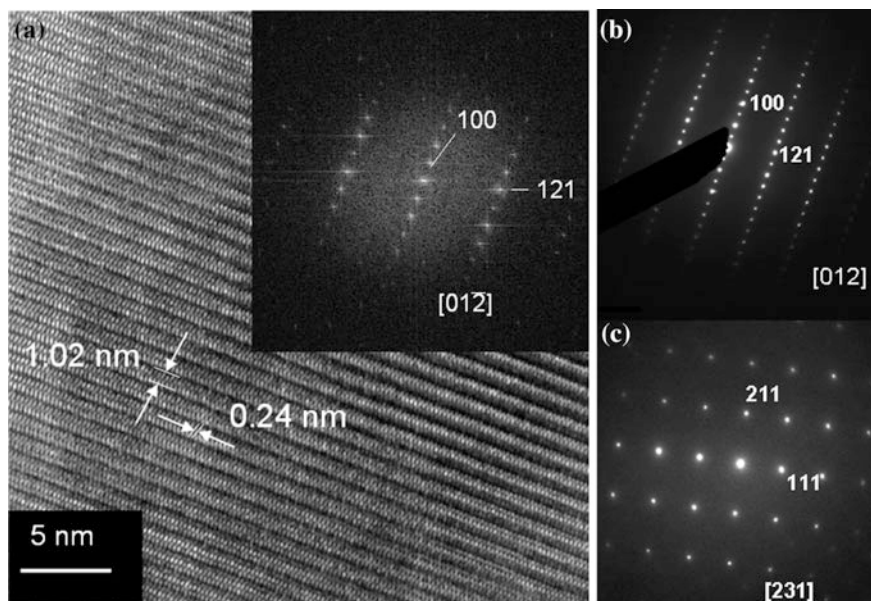


Fig. 23 **a** HRTEM image of LiNiPO_4 . The well-resolved lattice fringes indicate the crystallinity of the sample. The measured values of the lattice fringe spacing are indicated. Inset shows the FFT of the HRTEM image indicating the direction in which the crystallite was examined and lattice planes contributing to the diffraction. **b**, **c** SAED patterns of LiNiPO_4 . The assignments of diffraction maxima and the direction of view are indicated

charged over 5.2 V [137–139, 149]. However, Wolfenstine and Allen [121] mentioned the electrochemical activity of LNP powders prepared by SSR method under high purity argon with addition of a thin layer of carbon coat. The voltammetry displayed an oxidation peak at ~ 5.3 V and a reduction peak at ~ 5.1 V.

Recently, Dimesso et al. [123, 150] have reported the preparation of LNP and LCP by a Pechini assisted sol–gel process that provides material exhibiting redox peaks at ~ 5.2 and ~ 4.9 V versus Li^0/Li^+ , respectively. Mg-substituted LNP/graphitic carbon foams composite was also synthesized by the same method that shows a discharge capacity of 126 mAh g^{-1} at C/10 rate by substituting 0.2 Mg for Ni [151]. Modifications of the local structure and lattice parameters in $\text{LiFe}_{1-y}\text{Ni}_y\text{PO}_4$ ($0 < x < 1$) olivine-type solid solutions have been studied by X-ray absorption spectroscopy (XAS) [152, 153]. Results indicate ordering of Li in the M1 site, and of Fe and Ni in the M2 site of the olivine structure. Ni doping is found to induce an anisotropic shrinking of the unit cell with both Fe and Ni six-coordinated with oxygens, occupying distorted octahedral sites. $\text{LiNi}_{1-x}\text{Cu}_x\text{PO}_4$ ($0 < x < 0.99$) samples were successfully synthesized by non-aqueous sol–gel method followed by microwave (MW) annealing were found to be electrocatalysts towards oxygen reduction which is apparently due to nanosized particles as obtained via MW annealing [152]. The solid solution $\text{LiNi}_x\text{Fe}_{1-x}\text{PO}_4$ ($0 < x < 1$)

synthesized via a solid-state reaction under Ar ambient shows lattice parameters following the Vegard's law but the formation of agglomerates reduces the specific capacity that cannot exceed 45 mAh g^{-1} [153].

8 Concluding Remarks

The use of lithiated frameworks has revolutionized the concept of lithium rechargeable batteries for high-power sources applied to hybrid electric vehicles (HEVs) and plug-in hybrid electric vehicles (PHEVs). To date, most interest has been focused on the LiFePO_4 phase, which is already in commercial use. In this chapter, we have provided the state-of-the-art of olivine (orthophosphate) compounds used as positive electrodes for the new generation of Li-ion batteries. The successful application of lithium iron phosphate has triggered great interest in the R&D of high-power batteries with remarkable safety concerns despite the fact that all these materials are insulators. Other olivine LiMPO_4 ($M=\text{Mn, Ni, Co}$) compounds, which have been identified as potential high-voltage cathode, are creating intensive studies both from scientific and technological points of view and some of the more prominent follow-up activities have been briefly discussed. Unfortunately these materials all suffer from a number of drawbacks that must be overcome before they can compete with LiFePO_4 . The limitation in capacity attributed to the diffusion-limited transfer of lithium across the two-phase interface $\text{LiMPO}_4\text{--MPO}_4$ as end members without much solubility has been overcome with reducing the particle at the nanometer scale and by painting them with conducting carbon. For example, LiMnPO_4 has poorer Li-ion conductivity than LiFePO_4 , LiNiPO_4 also exhibits extremely poor electronic conductivity and extremely low charge/discharge capacity. Nevertheless, the use of nanosized solid-state materials not only improves the power density, but also facilitates Li-ions insertion/extraction in/out of the storage materials, which improves the cycle life of these batteries. LiCoPO_4 (4.8 V) and LiNiPO_4 (5.2 V) with higher operating voltage are appealing for increasing the energy density. Owing to this, large room for improvements in the performances in Li-cells of LCP and LNP is expected by assessing the synthesis route, the coatings, the doping/substitution and the electrolyte additives in order to boost its ability to reversibly cycle lithium. However, the use of these cathodes requires challenges in the development of more stable and robust electrolytes.

References

1. Padhi K, Nanjundaswamy KS, Goodenough JB (1997) Phospho-olivines as positive-electrode materials for rechargeable lithium batteries. *J Electrochem Soc* 144:1188–1194
2. Padhi K, Nanjundaswamy KS, Masquelier C, Okada S, Goodenough JB (1997) Effect of structure on the $\text{Fe}^{3+}/\text{Fe}^{2+}$ redox couple in iron phosphates. *J Electrochem Soc* 144:1609–1613

3. Huang H, Yin SC, Nazar LF (2001) Approaching theoretical capacity of LiFePO_4 at room temperature at high rates. *Electrochem Solid State Lett* 4:A170–A172
4. Dominko D, Gaberscek M, Drofenik J, Bele M, Jamnik J (2003) Influence of carbon black distribution on performance of oxide cathodes for Li ion batteries. *Electrochim Acta* 48:3709–3716
5. Ravet N, Goodenough JB, Besner S, Simoneau M, Hovington P, Armand M (1999) Improved iron based cathode material. In: Proceedings of the 196th ECS meeting, Honolulu, Oct 1999, Extended Abstract no 127
6. Ravet N, Chouinard Y, Magnan JF, Besner S, Gauthier M, Armand M (2001) Electroactivity of natural and synthetic triphylite. *J Power Sources* 97:503–507
7. Bewlay SL, Konstantinov K, Wang GX, Dou SX, Liu HK (2004) Conductivity improvements to spray-produced LiFePO_4 by addition of a carbon source. *Mater Lett* 58:1788–1791
8. Julien CM, Mauger A, Ait-Salah A, Massot M, Gendron F, Zaghbi K (2007) Nanoscopic scale studies of LiFePO_4 as cathode material in lithium-ion batteries for HEV application. *Ionics* 13:395–411
9. Weppner W, Huggins R (1977) Determination of the kinetic parameters of mixed-conducting electrodes and applications to the system Li_3Sb . *J Electrochem Soc* 124:1569–1578
10. Chen Z, Dahn JR (2002) Reducing carbon in LiFePO_4/C composite electrodes to maximize specific energy, volumetric energy and tap density. *J Electrochem Soc* 149:A1184–A1189
11. Ravet N, Besner S, Simoneau M, Vallée A, Armand M, Magnan JF (2005) Electrode materials with high surface conductivity. US Patent 6,962,666, 8 Nov 2005
12. Nanjundaswamy KS, Padhi AK, Goodenough JB, Okada S, Ohtsuka H, Arai H, Yamaki J (1996) Synthesis, redox potential evaluation and electrochemical characteristics of NASICON-related-3D framework compounds. *Solid State Ionics* 92:1–10
13. Pahdi AK, Manivannan M, Goodenough JB (1998) Tuning the position of the redox couples in materials with NASICON structure by anionic substitution. *J Electrochem Soc* 145:1518–1520
14. Manthiram A, Goodenough JB (1989) Lithium insertion into $\text{Fe}_2(\text{SO}_4)_3$ frameworks. *J Power Sources* 26:403–408
15. Nyten A, Abouimrane A, Armand M, Gustafsson T, Thomas JO (2005) Electrochemical performance of $\text{Li}_2\text{FeSiO}_4$ as a new Li-battery cathode material. *Electrochem Commun* 7:156–160
16. Barker J, Saidi MY, Swoyer JL (2003) Electrochemical insertion properties of the novel lithium vanadium fluorophosphate, LiVPO_4F . *J Electrochem Soc* 150:A1394–A1398
17. Zaghbi K, Mauger A, Julien CM (2012) Overview of olivines in lithium batteries for green transportation and energy storage. *J Solid State Electrochem* 16:835–845
18. Julien CM, Zaghbi K, Mauger A, Groult H (2012) Enhanced electrochemical properties of LiFePO_4 as positive electrode of Li-ion batteries for HEV application. *Adv Chem Eng Sci* 2:321–329
19. Fergus JW (2010) Recent developments in cathode materials for lithium ion batteries. *J Power Sources* 195:939–954
20. Ait-Salah A, Mauger A, Julien CM, Gendron F (2006) Nanosized impurity phases in relation to the mode of preparation of LiFeO_4 effects. *Mater Sci Eng, B* 129:232–244
21. Ait-Salah A, Mauger A, Zaghbi K, Goodenough JB, Ravet N, Gauthier M, Gendron F, Julien CM (2006) Reduction of Fe^{3+} impurities in LiFePO_4 from the pyrolysis of organic precursor used for carbon deposition. *J Electrochem Soc* 153:A1692–A1701
22. Zaghbi K, Dontigny M, Charest P, Labrecque JF, Guerfi A, Kopeć M, Mauger A, Gendron F, Julien CM (2010) LiFePO_4 : from molten ingot to nanoparticles with high-rate performance in Li-ion batteries. *J Power Sources* 195:8280–8288
23. Brochu F, Guerfi A, Trottier J, Kopeć M, Mauger A, Groult H, Julien CM, Zaghbi K (2012) Structure and electrochemistry of scaling nano C- LiFePO_4 synthesized by hydrothermal route: complexing agent effect. *J Power Sources* 214:1–6

24. VEDIAPPAN K, GUERFI A, GARIÉPY V, DEMOPOULOS GP, HOVINGTON P, TROTTIER J, MAUGER A, JULIEN CM, ZAGHIB K (2014) Stirring effect in hydrothermal synthesis of C-LiFePO₄. *J Power Sources* 266:99–106
25. Herle PS, Ellis B, Coombs N, Nazar LF (2004) Nano-network electronic conduction in iron and nickel olivine phosphates. *Nat Mater* 3:147–152
26. Ait-Salah A, Dodd J, Mauger A, Yazami R, Gendron F, Julien CM (2006) Structural and magnetic properties of LiFePO₄ and lithium extraction effects. *Z Allg Inorg Chem* 632:1598–1605
27. Ellis BL, Lee KT, Nazar LF (2010) Positive electrode materials for Li-ion and Li-batteries. *Chem Mater* 22:691–714
28. Ravet N, Gauthier M, Zaghib K, Goodenough JB, Mauger A, Gendron F, Julien CM (2007) Mechanism of the Fe³⁺ reduction at low temperature for LiFePO₄ synthesis from polymeric precursor. *Chem Mater* 19:2595–2602
29. Laffont L, Delacourt C, Gibot P, Wu MY, Kooyman P, Masquelier C, Tarascon JM (2006) Study of the LiFePO₄/FePO₄ two-phase system by high-resolution electron energy loss spectroscopy. *Chem Mater* 18:5520–5529
30. Zaghib K, Mauger A, Gendron F, Julien CM (2008) Surface effects on the physical and electrochemical properties of thin LiFePO₄ particles. *Chem Mater* 20:462–469
31. Yang S, Zavajil PY, Whittingham MS (2001) Hydrothermal synthesis of lithium iron phosphate cathodes. *Electrochem Commun* 3:505–508
32. Sato M, Tajimi S, Okawa H, Uematsu K, Toda K (2002) Preparation of iron phosphate cathode material of Li₃Fe₂(PO₄)₃ by hydrothermal reaction and thermal decomposition processes. *Solid State Ionics* 152–153:247–251
33. Dokko K, Koizumi S, Kanamura K (2006) Electrochemical reactivity of LiFePO₄ prepared by hydrothermal method. *Chem Lett* 35:338–339
34. Dokko K, Koizumi S, Shiraishi K, Kanamura K (2007) Electrochemical properties of LiFePO₄ prepared via hydrothermal route. *J Power Sources* 165:656–659
35. Jin B, Gu HB (2008) Preparation and characterization of LiFePO₄ cathode materials by hydrothermal method. *Solid State Ionics* 178:1907–1914
36. Murugan AV, Muraliganth T, Manthiram A (2009) One-pot microwave-hydrothermal synthesis and characterization of carbon-coated LiMPO₄ (M=Mn, Fe, and Co) cathodes. *J Electrochem Soc* 156:A79–A83
37. Kim DH, Kim J (2006) Synthesis of LiFePO₄ nanoparticles in polyol medium and their electrochemical properties. *Electrochem Solid State Lett* 9:A439–A442
38. Kim DH, Kim J (2007) Synthesis of LiFePO₄ nanoparticles and their electrochemical properties. *J Phys Chem Solids* 68:734–737
39. Kim DH, Lim JS, Kang JW, Kim EJ, Ahn HY, Kim J (2007) A new synthesis route to nanocrystalline olivine phosphates and their electrochemical properties. *J Nanosci Nanotechnol* 7:3949–3953
40. Azib T, Ammar S, Nowak S, Lau-Truing S, Groult H, Zaghib K, Mauger A, Julien CM (2012) Crystallinity of nano C-LiFePO₄ prepared by the polyol process. *J Power Sources* 217:220–228
41. Saravanan K, Reddy MV, Balaya P, Gong H, Chowdari BVR, Vittal JJ (2009) Storage performance of LiFePO₄ nanoplates. *J. Mater. Chem* 19:605–610
42. Yang H, Wu XL, Cao MH, Guo YG (2009) Solvothermal synthesis of LiFePO₄ hierarchically dumbbell-like microstructures by nanoplate self-assembly and their application as a cathode material in lithium-ion batteries. *J Phys Chem C* 113:3345–3351
43. Arcon D, Zorko A, Dominko R, Jaglicic Z (2004) A comparative studies of magnetic properties of LiFePO₄ and LiMnPO₄. *J Phys C Condens Matter* 16:5531–5548
44. Geller S, Durand JL (1960) Refinement of the structure of LiMnPO₄. *Acta Crystallogr* 13:325–329
45. Santorrio RP, Newnham RE (1987) Antiferromagnetism in LiFePO₄. *Acta Crystallogr* 22:344–347

46. Streltsov VA, Belokoneva EL, Tsirelson VG, Hansen NK (1993) Multipole analysis of the electron density in triphylite LiFePO_4 using X-ray diffraction data. *Acta Crystallogr B* 49:147–153
47. Rousse G, Rodriguez-Carvajal J, Patoux S, Masquelier C (2003) Magnetic structures of the triphylite LiFePO_4 and its delithiated form FePO_4 . *Chem Mater* 15:4082–4090
48. Losey A, Rakovan J, Huges J, Francis CA, Dyar MD (2004) Structural variation in the lithiophilite-triphylite series and other olivine-group structures. *Canad Mineral* 42:1105–1108
49. Andersson AS, Thomas JO (2001) The source of first-cycle capacity loss in LiFePO_4 . *J Power Sources* 97–98:498–502
50. Nyten A, Thomas JO (2006) A neutron powder diffraction study of $\text{LiCo}_x\text{Fe}_{1-x}\text{PO}_4$ for $x = 0, 0.25, 0.40, 0.60$ and 0.75 . *Solid State Ionics* 177:1327–1330
51. Beale AM, Sankar G (2002) Following the structural changes in iron phosphate catalysts by in situ combined XRD/QuEXAFS technique. *J Mater Chem* 12:3064–3072
52. Yamada A, Chung SC, Hinokuma K (2001) Optimized LiFePO_4 for lithium battery cathodes. *J Electrochem Soc* 148:A224–A229
53. Andersson AS, Thomas JO (2001) The source of first-cycle capacity loss in LiFePO_4 . *J Power Sources* 97–98:498–502
54. Julien CM, Zaghib K, Mauger A, Massot M, Ait-Salah A, Selmane M, Gendron F (2006) Characterization of the carbon-coating onto LiFePO_4 particles used in lithium batteries. *J Appl Phys* 100:063511
55. Ait-Salah A, Jozwiak P, Zaghib K, Garbarczyk J, Gendron F, Mauger A, Julien CM (2006) FTIR features of lithium-iron phosphates as electrode materials for rechargeable lithium batteries. *Spectrochim Acta A* 65:1007–1013
56. Julien CM, Ait-Salah A, Gendron F, Morhange JF, Mauger A, Ramana CV (2006) Microstructure of LiXPO_4 ($X=\text{Ni, Co, Mn}$) prepared by solid-state chemical reaction. *Scripta Mater* 55:1179–1182
57. Burba CM, Frech R (2006) In situ transmission FTIR spectroelectrochemistry: A new technique for studying lithium batteries. *Electrochem Acta* 52:780–785
58. Paques-Ledent MT, Tarte P (1974) Vibrational studies of olivine-type compounds—II orthophosphates, -arsenates and -vanadates $A^IB^{II}X^VO_4$. *Spectrochim Acta, Part A* 30: 673–689
59. Ait-Salah A, Zaghib K, Mauger A, Gendron F, Julien CM (2006) Magnetic studies of the carbothermal effect on LiFePO_4 . *Phys Status Solidi A* 203:R1–R3
60. Doeff MM, Hu Y, McLarnon F, Kostecki R (2003) Effect of surface carbon structure on the electrochemical performance of LiFePO_4 . *Electrochem Solid State Lett* 6:A207–A209
61. Arnold G, Garche J, Hemmer R, Ströbele S, Vogler C, Wohlfahrt-Mehrens M (2003) Fine-particle lithium iron phosphate LiFePO_4 synthesized by a new low-cost aqueous precipitation technique. *J Power Sources* 119–121:247–251
62. Axmann P, Stinner C, Wohlfahrt-Mehrens M, Mauger A, Gendron F, Julien CM (2009) Non-stoichiometric LiFePO_4 : defects and related properties. *Chem Mater* 21:1636–1644
63. Zaghib K, Dontigny M, Charest P, Labrecque JF, Guerfi A, Kopec M, Mauger A, Gendron F, Julien CM (2008) Aging of LiFePO_4 upon exposure to H_2O . *J Power Sources* 185:698–710
64. Porcher W, Moreau P, Lestriez B, Jouanneau S, Guyomard D (2008) *Electrochim Solid State Lett* 11:A4–A8
65. Zaghib K, Ravet N, Gauthier M, Gendron F, Mauger A, Goodenough JB, Julien CM (2006) Optimized electrochemical performance of LiFePO_4 at 60°C with purity controlled by SQUID magnetometry. *J Power Sources* 163:560–566
66. Bramnik NN, Ehrenberg H (2008) Precursor-based synthesis and electrochemical performance of LiMnPO_4 . *J Alloys Compd* 464:259–264
67. Rissouli K, Benkhoulja K, Ramos-Barrado JR, Julien C (2003) Electrical conductivity in lithium orthophosphates. *Mater Sci Eng B* 98:185–189
68. Drezen T, Kwon NH, Bowen P, Teerlinck I, Isono M, Exnar I (2007) Effect of particle size on LiMnPO_4 cathodes. *J Power Sources* 174:949–953

69. Wang D, Buqa H, Crouzet M, Deghenghi G, Drezen T, Exnar I, Kwon NH, Miners J, Poletto L, Gratzel M (2009) High-performance, nano-structured LiMnPO_4 synthesized via a polyol method. *J Power Sources* 189:624–628
70. Martha SK, Markovsky B, Grinblat J, Gofer Y, Haik O, Zinigrad E, Aurbach D, Drezen T, Wang D, Deghenghi G, Exnar I (2009) LiMnPO_4 as an advanced cathode material for rechargeable lithium batteries. *J Electrochem Soc* 156:A541–A552
71. Liu JL, Hu DG, Huang T, Yu AS (2012) Synthesis of flower-like LiMnPO_4/C with precipitated $\text{NH}_4\text{MnPO}_4 \cdot \text{H}_2\text{O}$ as precursor. *J Alloys Compd* 518:58–62
72. Bakenov Z, Taniguchi I (2010) $\text{LiMg}_x\text{Mn}_{1-x}\text{PO}_4/\text{C}$ cathodes for lithium batteries prepared by a combination of spray pyrolysis with wet ballmilling. *J Electrochem Soc* 157:A430–A436
73. Doan TNL, Bakenov Z, Taniguchi I (2010) Preparation of carbon coated LiMnPO_4 powders by a combination of spray pyrolysis with dry ball-milling followed by heat treatment. *Adv Powder Technol* 21:187–196
74. Xiao J, Xu W, Choi D, Zhang J (2010) Synthesis and characterization of lithium manganese phosphate by a precipitation method. *J Electrochem Soc* 157:A142–A147
75. Fujimoto D, Lei Y, Huang ZH, Kang F, Kawamura J (2014) Synthesis and electrochemical performance of LiMnPO_4 by hydrothermal method. *Int J Electrochem* 2014:768912
76. Devaraju MK, Honma I (2012) Hydrothermal and solvothermal process towards development of LiMPO_4 ($\text{M}=\text{Fe}, \text{Mn}$) nanomaterials for lithium-ion batteries. *Adv Ener Mater* 2:284–297
77. Zhou F, Zhu P, Fu X, Chen R, Sun R, Wong C (2014) Comparative study of LiMnPO_4 cathode materials synthesized by solvothermal methods using different manganese salts. *Cryst Eng Comm* 16:766–774
78. Wang D, Buqa H, Crouzet M et al (2009) High-performance, nano-structured LiMnPO_4 synthesized via a polyol method. *J Power Sources* 189:624–628
79. Bakenov Z, Taniguchi I (2011) LiMnPO_4 olivine as a cathode for lithium batteries. *Open Mater Sci J* 5:222–227
80. Kwon NH, Fromm KM (2012) Enhanced electrochemical performance of <30 nm thin LiMnPO_4 nanorods with reduced amount of carbon as a cathode for lithium ion batteries. *Food Chem* 133:1435–1440
81. Kumar PR, Venkateswarlu M, Misra M, Mohanty AK, Satyanarayana N (2011) Carbon coated LiMnPO_4 nanorods for lithium batteries. *J Electrochem Soc* 158:A227–A230
82. Yuan LF, Ge LL, Shen YH, Zhang H, Wang CP, Xie AJ (2013) Synthesis and electrochemical properties of Cu-doped LiMnPO_4/C nanorods as cathode materials of lithium-ion batteries. *J Nano Res* 25:1–7
83. Pivko M, Bele M, Tchernychova E, Logar NZ, dominko R, Gaberscek M (2012) Synthesis of nanometric LiMnPO_4 via a two-step technique. *Chem Mater* 24:1041–1047
84. Kim TA, Park HS, Lee MH, Lee SY, Song HK (2012) Restricted growth of LiMnPO_4 nanoparticles evolved from a precursor seed. *J Power Sources* 210:1–6
85. Kim J, Seo DH, Kim SW, Park YU, Kang K (2010) Mn based olivine electrode material with high power and energy. *Chem Commun* 46:1305–1307
86. Lee KT, Kan WH, Nazar LF (2009) Proof of intercrystallite ionic transport in LiMPO_4 electrodes ($\text{M}=\text{Fe}, \text{Mn}$). *J Am Chem Soc* 131:6044–6045
87. Choi D, Wang D, Bae IT, Xiaot J, Nie Z, Wang W, Yiswanathan Y, Lee Y, Zhang JG, Graff G, Yang Z, Liu J (2010) LiMnPO_4 nanoplate grown via solid-state reaction in molten hydrocarbon for Li-ion battery cathode. *Nano Lett* 10(8):2799–2805
88. Li L, Liu J, Chen L, Xu H, Yang J, Qian Y (2013) Effect of different carbon sources on the electrochemical properties of rod-like LMP/C nanocomposites. *RSC Adv* 3:6847–6852
89. Zhao M, Fu Y, Xu N, Li G, Wu M, Gao X (2014) High performance LiMnPO_4/C prepared by a crystallite size control method. *J Mater Chem A* 2:15070–15077
90. Chen G, Richardson TJ (2010) Thermal instability of olivine-type LiMnPO_4 cathodes. *J Power Sources* 195:1221–1224
91. Zhong S, Xu Y, Li Y, Zeng H, Li W, Wang J (2012) Synthesis and electrochemical performance of LiMnPO_4/C composites cathode materials. *Rare Met* 31:474–478

92. Wang L, Sun W, Li J, Gao J, He X, Jiang C (2012) Synthesis of electrochemically active LiMnPO_4 via $\text{MnPO}_4 \cdot \text{H}_2\text{O}$ with different morphology prepared by facile precipitation. *Int J Electrochem Sci* 7:3591–3600
93. Barpanda P, Djellab K, Recham N, Armand M, Tarascon JM (2011) Direct and modified ionothermal synthesis of LiMnPO_4 with tunable morphology for rechargeable Li-ion batteries. *J Mater Chem* 21:10143–10152
94. Murugan AV, Muraliganth T, Ferreira PJ, Manthiram A (2009) Dimensionally modulated, single-crystalline LiMPO_4 (M=Mn, Fe Co, and Ni) with nano-thumblike shapes for high-power energy storage. *Inorg Chem* 48:946–952
95. Kosova NV, Devyatkina ET, Ancharov AI, Markov AV, Karnaushenko DD, Makukha VK (2012) Structural studies of nanosized $\text{LiFe}_{0.5}\text{Mn}_{0.5}\text{PO}_4$ under cycling by in situ synchrotron diffraction. *Solid State Ionics* 225:564–569
96. Wang H, Yang Y, Liang Y, Cui LF, Casalongue HS, Li Y, Hong G, Cui Y, Da H (2011) $\text{LiMn}_{1-x}\text{Fe}_x\text{PO}_4$ nanorods grown on graphene sheets for ultrahigh-rate-performance lithium ion batteries. *Angew Chem Int Ed* 50:7364–7368
97. Kopec M, Yamada A, Kobayashi G, Nishimura S, Kanno R, Mauger A, Gendron F, Julien CM (2009) Structural and magnetic properties of $\text{Li}_x(\text{Mn}_y\text{Fe}_{1-y})\text{PO}_4$ electrode materials for Li-ion batteries. *J Power Sources* 189:1154–1163
98. Zaghib K, Mauger A, Gendron F, Massot M, Julien CM (2008) Insertion properties of $\text{LiFe}_{0.5}\text{Mn}_{0.5}\text{PO}_4$ electrode materials for Li-ion batteries. *Ionics* 14:371–376
99. Gardiner GR, Islam MS (2010) Anti-site defects and ion migration in the $\text{LiFe}_{0.5}\text{Mn}_{0.5}\text{PO}_4$ mixed-metal cathode material. *Chem Mater* 22:1242–1248
100. Trottier J, Mathieu MC, Guerfi A, Zaghib K, Mauger A, Julien CM (2013) $\text{LiMn}_y\text{Fe}_{1-y}\text{PO}_4$ ($0.5 \leq y \leq 0.8$) cathode materials grown by hydrothermal route: electrochemical performance. *ECS Trans* 50–24:109–114
101. Hong Y, Tang Z, Hong Z, Zhang Z (2014) $\text{LiMn}_{1-x}\text{Fe}_x\text{PO}_4$ ($x = 0, 0.1, 0.2$) nanorods synthesized by a facile solvothermal approach as high performance cathode materials for lithium-ion batteries. *J Power Sources* 248:655–659
102. Truong QD, Devaraju MK, Ganbe Y, Tomai T, Honma I (2013) Controlling the shape of LiCoPO_4 nanocrystals by supercritical fluid process for enhanced energy storage properties. *Sci Rep* 4:3975
103. Wang F, Yang J, Nuli Y, Wang J (2011) Novel hedgehog-like 5 V LiCoPO_4 positive electrode material for rechargeable lithium battery. *J Power Sources* 196:4806–4810
104. Su J, Wei BQ, Rong JP, Yin WY, Ye ZX, Tian XQ, Ren L, Cao MH, Hu CW (2011) A general solution-chemistry route to the synthesis LiMPO_4 (M=Mn, Fe and Co) nanocrystals with [010] orientation for lithium ion batteries. *J Solid State Chem* 184:2909–2919
105. Wolfenstine J, Allen J (2004) LiNiPO_4 – LiCoPO_4 solid solutions as cathodes. *J Power Sources* 136:150–153
106. Ni J, Gao L, Lu L (2013) Carbon coated lithium cobalt phosphate for Li-ion batteries: Comparison of three coating techniques. *J Power Sources* 221:35–41
107. Wolfenstine J, Read J, Allen J (2007) Effect of carbon on the electronic conductivity and discharge capacity LiCoPO_4 . *J Power Sources* 163:1070–1073
108. Wolfenstine J, Lee U, Poesse B, Allen J (2005) Effect of oxygen partial pressure on the discharge capacity of LiCoPO_4 . *J Power Sources* 144:226–230
109. Wolfenstine J, Poesse B, Allen J (2004) Chemical oxidation of LiCoPO_4 . *J Power Sources* 138:281–282
110. Okada S, Sawa S, Egashira M, Yamaki JI, Tabuchi M, Kageyama H, Konishi T, Yoshino A (2001) Cathode properties of phospho-olivine LiMPO_4 for lithium secondary batteries. *J Power Sources* 97–98:430–432
111. Bramnik NN, Bramnik KG, Baetz C, Ehrenberg H (2005) Study of the effect of different synthesis routes on Li extraction–insertion from LiCoPO_4 . *J Power Sources* 145:74–81
112. Wolfenstine J (2006) Electrical conductivity of doped LiCoPO_4 . *J Power Sources* 158:1431–1435

113. Wang F, Yang J, Li YN, Wang J (2011) Novel hedgehog-like 5 V LiCoPO_4 positive electrode material for rechargeable lithium battery. *J Power Sources* 196:4806–4810
114. Nakayama M, Goto S, Uchimoto Y, Wakihara M, Kitayama Y, Miyana T, Watanabe I (2005) X-ray absorption spectroscopic study on the electronic structure of $\text{Li}_{1-x}\text{CoPO}_4$ electrodes as 4.8 V positive electrodes for rechargeable lithium ion batteries. *J Phys Chem B* 109:11197–11203
115. Bramnik NN, Nikolowski K, Baetz C, Bramnik KG, Ehrenberg H (2007) Phase transition occurring upon lithium insertion-extraction of LiCoPO_4 . *Chem Mater* 19:908–915
116. Zhao Y, Wang S, Zhao C, Xia D (2009) Synthesis and electrochemical performance of LiCoPO_4 micron-rods by dispersant-aided hydrothermal method for lithium ion batteries. *Rare Met* 28:117–121
117. Bramnik NN, Nikolowski K, Trots DM, Ehrenberg H (2008) Thermal stability of LiCoPO_4 cathodes. *Electrochem Solid State Lett* 11:A89–A93
118. Jang IC, Lim HH, Lee SB, Karthikeyan K, Aravindan V, Kang KS, Yoon WS, Cho WI, Lee YS (2010) Preparation of LiCoPO_4 and LiFePO_4 coated LiCoPO_4 materials with improved battery performance. *J Alloys Compd* 497:321–324
119. Bramnik NN, Nikolowski K, Trots DM, Ehrenberg H (2008) Thermal stability of LiCoPO_4 cathodes. *Electrochem Solid State Lett* 11:A89–A93
120. Aravindan V, Cheah YL, Chui Ling WC, Madhavi S (2012) Effect of LiBOB additive on the electrochemical performance of LiCoPO_4 . *J Electrochem Soc* 159:A1435–A1439
121. Wolfenstine J, Allen J (2005) $\text{Ni}^{3+}/\text{Ni}^{2+}$ redox potential in LiNiPO_4 . *J Power Sources* 142:389–390
122. Karthickprabhu S, Hirankumar G, Maheswaran A, Daries-Bella RS, Sanjeeviraja C (2014) Structural, morphological, vibrational and electrical studies on Zn doped nanocrystalline LiNiPO_4 . *Mater Sci Forum* 781:145–153
123. Dimesso L, Becker D, Spanheimer C, Jaegermann W (2012) Investigation of graphitic carbon foams/ LiNiPO_4 composites. *J Solid State Electrochem* 16:3791–3798
124. Piana M, Arrabito M, Bodoardo S, D'Epifanio A, Satolli D, Croce F, Scrosati B (2002) Characterization of phospho-olivines as materials for Li-ion cells cathodes. *Ionics* 8:17–26
125. Julien CM, Mauger A, Zaghib K, Veillette R, Groult H (2012) Structural and electronic properties of the LiNiPO_4 orthophosphate. *Ionics* 18:625–633
126. Herle PS, Ellis B, Coombs N, Nazar LF (2004) Nano-network electronic conduction in iron and nickel olivine phosphates. *Nat Mater* 3:147–152
127. Sugiyama J, Nozaki H, Harada M, Kamazawa K, Ikeda Y, Miyake Y, Ofer O, Mansson M, Ansaldi EJ, Chow KH (2012) Diffusive behaviour in LiMPO_4 with $\text{M}=\text{Fe}, \text{Co}, \text{Ni}$ probed by muon-spin relaxation. *Phys Rev B* 85:054111
128. Wang D, Xiao J, Xu W, Zhang JG (2010) Investigation of LiNiPO_4 as a cathode material for lithium ion battery. The 15th international meeting on lithium batteries, IMLB2010, abstract no°372
129. Minakshi M, Singh P, Ralph D, Appadoo D, Blackford M, Ionescu M (2012) Structural characteristics of olivine $\text{Li}(\text{Mg}_{0.5}\text{Ni}_{0.5})\text{PO}_4$ via TEM analysis. *Ionics* 18:583–590
130. Ramana CV, Ait-Salah A, Utsunomiya S, Becker U, Mauger A, Gendron F, Julien CM (2006) Structural characteristics of lithium nickel phosphate olivine studied using analytical electron microscopy and raman spectroscopy. *Chem Mater* 18:3788–3794
131. Cheruku R, Govindaraj G (2014) Structural and electrical conductivity studies of nanocrystalline olivine type LiNiPO_4 material. *Int J ChemTech Res* 6:2017–2201
132. Goñi A, Lezama L, Barberis GE, Pizarro JL, Arriortua MI, Rojo T (1996) Magnetic properties of the LiMPO_4 ($\text{M}=\text{Co}, \text{Ni}$) compounds. *J Magn Magn Mater* 164:251–255
133. Santoro RP, Segal DJ, Newnham RE (1966) Magnetic properties of LiCoPO_4 and LiNiPO_4 . *J Phys Chem Solids* 27:1192–1193
134. Toft-Petersen R, Jensen J, Jensen TBS, Andersen NH, Christensen NB, Niedemayer C, Kenzelmann M, Skoulatos M, Le MD, Lefmann K, Hensen SR, Li J, Zarestky JL, Vaknin D (2011) High-field magnetic phase transition and spin excitations in magnetoelectric LiNiPO_4 . *Phys Rev B* 84:054408

135. Vaknin D, Zarestky JL, Rivera JP, Schmid H (2004) Commensurate-incommensurate magnetic phase transition in magnetoelectric single crystal LiNiPO_4 . *Phys Rev Lett* 92:207201
136. Fomin VI, Gnezdilov VP, Kurnosov VS, Peschanskii AV, Yeremenko AV, Schmid H, Rivera JP, Gentil S (2002) Raman scattering in a LiNiPO_4 single crystal. *Low Temp Phys* 28:203–209
137. Ficher CAJ, Prieto VMH, Islam MS (2008) Lithium battery materials LiMPO_4 (M=Mn, Fe, Co and Ni): insights into defect association, transport mechanisms and doping behaviour. *Chem Mater* 20:5907–5915
138. Garcia-Moreno O, Alvarez-Vega M, Garcia-Alvarado F, Garcia-Jaca J, Garcia-Amores JM, Sanjuan ML, Amador U (2001) Influence of the structure on the electrochemical performance of lithium transition metal phosphates as cathodic materials in rechargeable lithium batteries: a new high-pressure form of LMPO_4 (M=Fe and Ni). *Chem Mater* 13:1570–1576
139. Zhou F, Cococcioni M, Kang K, Ceder G (2004) The Li intercalation potential of LiMPO_4 and LiMSiO_4 olivines with M=Fe, Mn Co, Ni. *Electrochem Commun* 6:1144–1148
140. Howard WF, Spotnitz RM (2007) Theoretical evaluation of high-energy lithium metal phosphate cathode materials in Li-ion batteries. *J Power Sources* 165:887–891
141. Chevrier VL, Ong SP, Armiento R, Chan MKY, Ceder G (2010) Hybrid density functional calculations of redox potentials and formation energies of transition metal compounds. *Phys Rev B* 82:075122
142. Rommel SM, Schall N, Brünig C, Wehrich R (2014) Challenges in the synthesis of high voltage electrode materials for lithium-ion batteries: a review on LiNiPO_4 . *Monatsh Chem* 145:385–404
143. Kausarjanjua N, Mumtaz M, Yabuq A, Sabahat S, Mujtaba A (2014) Electrocatalytic activity of LiNiPO_4 and the copper doped analogues towards oxygen reduction. *Nucleus* 51:109–115
144. Yang J, Xu JJ (2006) Synthesis and characterization of carbon-coated lithium transition metal phosphates LiMPO_4 (M=Fe, Mn Co, Ni) prepared via nonaqueous sol-gel route. *J Electrochem Soc* 153:A716–A723
145. Tsai A (2011) Synthesis and characterization of LiNiPO_4 nanocrystals via microemulsion method as a new class of electrocatalyst for oxygen reduction. Master's thesis, New Jersey Graduate School, New Brunswick
146. Prabu M, Selvasekarapandian S (2012) Dielectric and modulus studies of LiNiPO_4 . *Mater Chem Phys* 134:366–370
147. Gangulibabu DB, Kalaiselvi N, Jayaprakash N, Periasamy P (2009) CAM sol-gel synthesized LiMPO_4 (M=Co, Ni) cathodes for rechargeable lithium batteries. *J Sol-Gel Sci Technol* 49:137–144
148. Karthickprabhu S, Hirankumar G, Maheswaran A, Daries-Bella RS, Sanjeeviraja C (2013) Structural and conductivity studies on lanthanum doped LiNiPO_4 prepared by polyol method. In: Chowdari BVR, Kawamura J, Mizusaki J, Amezawa K (eds) *Proceedings of the 13th Asian conference on solid state ionics*, Sendai, Japan 17–20 July 2012, World Scientific, Singapore
149. Piana M, Arrabito M, Bodoardo S, D'Epifanio A, Satolli D, Croce F, Scrosati B (2002) Characterization of phospho-olivines as materials for Li-ion cells cathodes. *Ionics* 8:17–26
150. Dimesso L, Jacke S, Spanheimer C, Jaegermann W (2012) Investigation on LiCoPO_4 powders as cathode materials annealed under different atmospheres. *J Solid State Electrochem* 16:3911–3919
151. Dimesso L, Spanheimer C, Jaegermann W (2013) Effect of the Mg-substitution on the graphitic carbon foams— $\text{LiNi}_{1-y}\text{Mg}_y\text{PO}_4$ composites as possible cathodes materials for 5 V applications. *Mater Res Bull* 48:559–565
152. Tabassam L, Giuli G, Moretti A, Nobili F, Marassi R, Minicucci M, Gunnella R, Olivi L, DiCiccio A (2012) Structural study of LiFePO_4 - LiNiPO_4 solid solutions. *J Power Sources* 213:287–295
153. Qing R, Yang MC, Meng YS, Sigmund W (2013) Synthesis of $\text{LiNi}_x\text{Fe}_{1-x}\text{PO}_4$ solid solution as cathode materials for lithium ion batteries. *Electrochim Acta* 108:827–832

Rechargeable Batteries

Materials, Technologies and New Trends

Zhang, Z.; Zhang, S.S. (Eds.)

2015, IX, 712 p. 337 illus., Hardcover

ISBN: 978-3-319-15457-2